

An International  
Forum For  
The AE Science  
and Technology

# JOURNAL OF ACOUSTIC EMISSION

Vol.36/January-December 2019

Editors: M.A. Hamstad (AEWG) and G. Manthei (EWGAE)

- |          |   |  |
|----------|---|--|
| 36-001   | Receiving Sensitivities of Acoustic Emission Sensors: A data<br>Compilation   | Kanji Ono  |
| 36-001EX | Data File for 36-001  |  |
| 36-009   | Use of Acoustic Emission for Studying Ratcheting Behavior of 304LN Stainless<br>Steel Elbows  | C.K. Mukhopadhyay, T.K. Haneef, Suneel K. Gupta,<br>Vivek Bhasin, S. Vishnuvardhan, G. Raghava and P. Gandhi |
| 36-039   | Far-field wave propagation signals from pencil lead breaks on the open end<br>of a thick-walled layered cylinder: Part 1 Amplitudes and frequency content | M. A. Hamstad  |
| 36-051   | Far-field Wave Propagation Signals from Pencil Lead Breaks on the Open End<br>of a Thick-walled Layered Cylinder: Part 2 Modes of wave propagation        | M. A. Hamstad  |
| 36-071   | Detection of Defects in Spur Gears by Acoustic Emission Monitoring  | Swati Gautam and Naresh Tandon   |

Proceedings of International Conference on Acoustic Emission - 9  
Part I and II

Endorsed by  
AEWG  
and  
EWGAE

Published by  
Acoustic Emission Group  
Encino, CA USA  
©2019 Acoustic Emission Group



**9<sup>th</sup> INTERNATIONAL CONFERENCE ON ACOUSTIC EMISSION  
and  
61<sup>st</sup> ACOUSTIC EMISSION WORKING GROUP MEETING**



**Organized by: David Kosnik, Didem Ozevin and Valery Godinez,  
Compiled by: Didem Ozevin**

**9<sup>th</sup> INTERNATIONAL CONFERENCE ON ACOUSTIC EMISSION  
and  
61<sup>st</sup> ACOUSTIC EMISSION WORKING GROUP MEETING**

**June 17-20, 2019  
Chicago**

**PROGRAM COMMITTEE**

David Kosnik, Chair, CTL Group  
Didem Ozevin, University of Illinois Chicago  
Valery Godinez, MISTRAS Group

**EXECUTIVE COMMITTEE**

David Kosnik, Chair, CTL Group  
Didem Ozevin, Vice Chair, University of Illinois Chicago  
Valery Godinez, Secretary, MISTRAS Group  
Gang (Gary) Qi, Past-Chairman, University of Memphis  
Thomas F. Drouillard, Archivist  
Clinton R. Heiple, Treasurer, Metallurgical Consultant

**WEB SITE**

Jochen Vallen, Strategic Entrepreneurship Consulting

**SOCIETY WEB SITE**

[www.aewg.org](http://www.aewg.org)

**COVER Photograph**

Women in AE Networking Dinner (by Didem Ozevin)

**Publication Assistance**

Kanji Ono, University of California, Los Angeles

## **WELCOME REMARKS**

*On behalf of the organizing committee and international advisory board, I am pleased to welcome the global AE community to Chicago. As a native of the Chicago area, I am particularly glad to share “my city” with you.*

*Chicago is located in at the southern end of Lake Michigan in the central USA and enjoys direct airline service from major airports worldwide. While it is a young city by world standards (incorporated 1837), Chicago has risen to prominence as a global transportation hub, financial and manufacturing center, and locus for education and innovation at the heart of a metropolitan area of over nine million people.*

*The history of Chicago is intimately connected with technological and scientific innovations: reconstruction of the city following the Great Fire of 1871 included ten-story Home Insurance Building, the first tall building with a structural steel frame, and generally considered to be the world’s first skyscraper. In 1900, engineers reversed the flow of the Chicago River to protect water quality of Lake Michigan and enhance water transportation links through the region. The 110-story Sears Tower held the title of tallest building in the world from 1973 to 1998.*

*While Chicago does experience some lively weather, the appellation “Windy City” refers to the enthusiasm with which early twentieth century Chicagoans promoted their city. At the time of the AE meeting in mid-June, we can expect warm, sunny days with the heat moderated by the cooling breeze from Lake Michigan.*

*Most attractions within the city proper are accessible from the conference venue and suggested hotels by public transportation, taxi, or rideshare service – a rental car is not necessary.*

*In the summertime, the single best way to see the city is by boat cruise on the Chicago River and Lake Michigan. A number of options are available, from water taxi service to narrated and catered cruises. The conference banquet will be held on one of the latter.*

*In keeping with the city motto of Urbs in horto – “City in a Garden” – Chicago has many parks and public spaces, most notably a series of interconnected parks and paths along the Lake Michigan shoreline, and a ring of forest and prairie reserves around the city limits. Several national and state parks and reserves are located within a 1-2 hour drive from the city. In addition, nationwide domestic air connections are available from Chicago’s two airports (ORD and MDW), making Chicago a convenient hub for an extended visit to the USA.*

*I look forward to seeing you in Chicago!*

*David Kosnik  
Chairman, Acoustic Emission Working Group*

# **ICAE-9 & AEWG-61 Program**

MxD at 1415 N Cherry Ave, Chicago, IL 60642

## **Keynote – Dr. Hoda Azari**

Nondestructive Evaluation Program and Laboratory, Manager Asset Management and Construction Team  
Office of Infrastructure Research and Development, US Department of Transportation  
Federal Highway Administration

## **Keynote – Professor Joseph Rose**

Paul Morrow Professor Emeritus, Penn State University and CTO of FBS d/b/a Guidedwave

## **Keynote – Mauricio Calva**

Nondestructive Examination Expert, Chevron Energy Technology Company

### **Session 1-1 Fiber Optic AE Sensors and Dynamic Measurement**

Acoustic Modes in Optical Fibers for Lamb Wave and Acoustic Emission Detection

*Kara Peters, Junghyun Wee*

Fiber-optic acoustic emission sensor systems using fiber Bragg gratings

*Ming Han, Guigen Liu, Yupeng Zhu*

Development of Optical Fiber AE Sensor by FBG with WDM

*Hisafumi Asaue, Tomoki Shiotani, Katsufumi Hashimoto, Iori Yamamoto, Hidehiro Inaba*

Multichannel fiber laser acoustic emission sensor system

*Caitlin Williams, Meredith Hutchinson, Marriner Merrill, William Pogue, Peter Finkel, Geoffrey Cranch*

### **Session 1-2 Monitoring Composite Structures with AE**

Detection of Contaminants in Unidirectional Carbon Fiber Lay-ups

*Fady Barsoum, Isabel McBrayer*

Investigating the Structural Response of Composite Repairs under Cyclic Loading

*Fady Barsoum, Isabel McBrayer*

Damage Detection Through Fretting Emission in Center-Hole CFRP Skin of Cantilever Wing Box Under Constant-Moment Fatigue Loading

*Ryan J Neel, Jonathan Awerbuch, Tein-Min Tan, Didem Ozevin*

Damage Detection Through Acoustic Emission During Post-Fatigue Residual Strength Test of CFRP Skin of a Cantilevered Wingbox Under Constant-Moment Loading

*Ryan N Neel, Jonathan Awerbuch, Tein-Min Tan, Didem Ozevin*

Identifying the Presence and Position of Wheelflat via Acoustic Emission

*Okan Topcu*

### **Session 1-3 Monitoring in Service Systems with AE**

Development of damage detection method in type-III hydrogen pressure vessel by acoustic emission

*Takuma Matsuo, Hiroki Orito, Kotaro Hase*

Power Transformers monitoring

*Caricia Martinez, Arturo Nunez*

Increase uptime and plant reliability deploying asset monitoring solutions

*Arturo Nunez*

Infrastructure monitoring: solutions and examples

*Horst Trattning, Michael Hauserer*

Radar tower inspection using omnidirectional shear acoustic emission sensors

*Jason Philtron, Ronnie K. Miller, Steven Owens, Cody Borigo, Ward Fong*

### **Session 1-4 Signal Processing Methods**

Noise Tolerant and Wireless AE Measurement System for Process Monitoring

*Kaita Ito, Kazuki Takahashi, Manabu Enoki*

A deep learning-based two-step localization and characterization of acoustic emission sources in metallic panels using only one sensor, *Arvin Ebrahimkhanlou, Brennan Dubuc, Melanie Schneider, Salvatore Salamone*

Sensing and statistical analysis of acoustic emission due to crack rubbing/clapping in thin sheet metals  
*Roshan Joseph, Victor Giurgiutiu*

An Acoustic Emission IoT Framework for Monitoring, Data Management, Diagnostics and Prognostics  
*Krzysztof Mazur, Brian Wisner, Antonios Kotsos*

Application Of Acoustic Emission During Pressure Test Of Austenitic Steel Vessel  
*Václav Svoboda, František Žemlička*

### Session 2-1 Sensor Calibration Methods

Progress in Sensitivity Verification of AE Sensors

*Kanji Ono*

Experimental Characterization of PKBBI Sensor: the Low Power Flat Frequency Response, Broadband Acoustic Emission Sensor

*Hossein Saboonchi, Gonzalez Nunez Miguel*

Transmitters for the face-to-face sensor sensitivity verification - is their scatter tolerable?

*Hartmut Vallen*

Far-field wave propagation signals from pencil lead breaks on the open end of a thick-walled layered cylinder: Part 1 Amplitudes and frequency content

*Marvin Hamstad*

Far-field wave propagation signals from pencil lead breaks on the open end of a thick-walled layered cylinder: Part 2 Modes of wave propagation

*Marvin Hamstad*

### Session 2-2 AE in Materials Science

Acoustic Emission Information Discovery at the University of Illinois  
University of Illinois

*Mary C Schlembach, William H Mischo*

Study of dislocation dynamics of copper single crystals under cycling loading through acoustic emission and microstructural characterizations

*Gabriel L'Hote, Stephanie Deschanel, Sophie Cazottes, Maurine Montagnant*

Acoustic emission monitoring of post-installed shear connectors on steel bridges

*Arvin Ebrahimkhanlou, Salvatore Salamone, Arash Ebrahimkhanlou, Amir Reza Ghiami Azad, Kerry Kreitma, Todd Helwig, Eric Williamson, Michael Engelhardt*

On the Use of Acoustic Emission in Vibrations Testing or Progressive Failure Monitoring and Modeling

*Brian Wisner, Mira Shehu, Johnathon Kordell, Abhijit Dasgupta, Harsh Baid, Antonios Kotsos*

### Session 2-3 Additive Manufacturing Studies

Acoustic Emission Monitoring for Additively Manufactured Materials

*Brian Wisner, Emine Tekerek, Mir Shehu, Antonios Kotsos*

Monitoring Fracture Formation in Additively Manufactured Anisotropic Rocks

*Liyang Jiang, Hongkyu Yoon, Antonio Bobet, Laura J. Pyrak-Nolte*

Tensile Test of 3D Printed Specimens for Demonstrating the Performance of Acoustic Emission Measurement Systems

*Hironobu Yuki, Tomona Murata*

3D-printed anisotropic structure for switching elastic wave propagation

*Yoshihiro Mizutani, Ryuichiro Otonari, Takeshi Ashizawa, Akira Todoroki*

3D Printing for AE: Acoustic properties of 3D-Printed Materials and Development of Custom AE Fixtures' *Jaimy Juliano, David Kosnik, Richard Nordstrom, Shawn Anderson*

### Session 2-4 Monitoring Concrete Structures with AE

Evaluation of Damage Depth Inside Concrete Using Surface Wave Tomography

*Norihiko Ogura, Tomoki Shiotani*

Self-Healing Degradation of Asphalt Concrete Materials due to Cooling Cycles

*Behzad Behnia, Henrique Reis*

Application of Surface-Wave Tomography to Sealed Conditions of Repaired Cracks in Concrete

*Nobuhiro Okude, Tomoki Shiotani*

Internal damage detection of RC bridge decks with uniformly distributed elastic wave sources

*Hidefumi Takamine, Yuki Ueda, Kazuo Watabe, Katsufumi Hashimoto, Tomoki Shiotani*

### **Session 3-1 AE Theories and Modeling**

Modeling the Acoustic Emissions Produced by the Dynamic Fracture of a Glass Beam

*Valentin van Gemmeren, Jurg Dual*

Monitoring geochemically-induced fractures in synthetic rocks

*Chven A. Mitchell, Laura J. Pyrak-Nolte*

Omnidirectional shear acoustic emission sensor for improved location analysis

*Jason Philtron, Cody Borigo, Steven Owens, Ronnie K. Miller, Joseph L. Rose*

### **Session 3-2 Quantitative Studies of AE on Composite Materials**

Characterization of fiber break by quantitative acoustic emission in a model composite carbon/epoxy

*Zeina Hamam, Nathalie Godin, Claudio Fusco, Thomas Monnier*

AE Measurements and Analysis on a Layered Pressure Vessel

*Adrian Pollock, Miguel Gonzalez, Hossain Saboonchi*

Damage identification in composite tubes through acoustic emission monitoring

*Neha Chandarana, Emmanuel Ramasso, Constantinos Soutis, Matthieu Gresil*

Burst pressure prediction of composite vessels

*Markus Sause, Stefan Schmitt, Birte Hoeck, Andreas Monden*

Overview of Acoustic Emission in Monitoring Powder Technology

*Eric Serris, Ana Cameirao, Frederic Gruy, Jean-Michel Herri, Gerard Thomas*

### **Session 3-3 Testing Metallic Materials with AE**

Monitoring of fatigue cracking and damage of metallic materials through Acoustic Emission and Digital Image Correlation, *Stephanie Deschanel, Julien Rethore, Jerome Weiss*

Using machine learning to predict welding quality from airborne AE sensor data

*Kaiser Asif, Lu Zhang, Sybil Derrible, Ernesto Indacochea, Didem Ozevin, Brian Ziebart*

AE measurement during friction stir welding of flame-resistant magnesium alloy with simulated inclusions

*Kazuki Takahashi, Takayuki Shiraiwa, Manabu Enoki, Kaita Ito, Eitaro Yukutake*

Structural Health Monitoring of Mooring Chains Crack Initiation and Growth using Acoustic Emission

*Angela Angulo, Slim Soua, Tat-Hean Gan*

Characterization of Microdamage of Flexible Solar Cell under Fatigue Load using AE and LT Techniques

*Takahiro Matsueda, Shuichi Wakayama, Kosuke Nakahara, Akihiro Takano*

### **Session 3-4 Civil Infrastructure Applications**

Acoustic Emission Measurements of Detensioning and Transport of Prestressed Reinforced Concrete Bridge Girders

*Dryver Huston, Robert Worley II, Mandar Dewoolkar, Tian Xia, Daniel Orfeo*

Application of Non-Contact Laser Impact with AE Analysis and Tomography Technique for Damage Identification in Concrete, *Tomoki Shiotani, Katsufumi Hashimoto, Masaharu Nishikino, Katsuhiro Mikami*

Damage Quantification of RC decks by Means of Rain-Induced AE Excitations and Source Location Bias

*Katsufumi Hashimoto, Tomoki Shiotani, Kazuo Watabe, Hidefumi Takamine*

Development of prestressed concrete bridge tendon damage diagnosis system using acoustic emission technique

*Dong-Woo Seo, Ga-Young Kim, Ki-Tae Park, Dong-Hyun Kim, Yoon-Gi Hong*

Development of Structural Health Monitoring Technology for Internal Tendon of PSC Bridge Using Acoustic Emission Technology, *Dong-Hyun Kim, Yoon-Gi Hong, Dong-Woo Seo, Ki-Tae Park*

### **Session 4-1 Advances in AE Sensors and Signal Processing**

A new time-domain feature (RKM) for Acoustic Emission transient signal processing

*Ronnie Miller, Jason Philtron*

Applying Location Accuracy Refinement to Simulated Location Testing Results

*David Kosnik, Richard Nordstrom*

Multi-frequency MEMS Acoustic Emission Sensor

*Hanie Kazari, Didem Ozevin*

Off-the-Shelf Tools for Generalized, Automated Large-Scale Location Accuracy Refinement

*Horst Trattnig, David Kosnik, Richard Nordstrom*

## Session 4-2 Advanced Applications of AE

Acoustic Emission Characterization of a Composite Overwrapped Pressure Vessel as a Structural Health Monitoring Method  
*Behnoush Golchinfar, Miguel Gonzalez Nunez, Patsi Francis*

A comparison study of Vibro-Acoustic Modulation technique and Conventional AE

*Behnoush Golchinfar, Majid Ramezani Goldyani, Hossain Saboonchi, Dimitri Donskoy*

Use of Acoustic Emission for identifying Gas-Liquid mixing regime in agitated vessel applying machine learning

*Giuseppe Forte, Federico Alberini, Mark Simmon, Hugh Stitt*

Phased Acoustic Emission Sensor Array for Determining Radial and Axial Position of Defects in Pipe-like Structures

*Lu Zhang, Chen Enpei, Gorkem Okudan, Didem Ozevin*

## **Papers not presented**

Acoustic Emission in Process of Thermal Decomposition of Potassium Hydrogen Carbonate Crystals,

*Shavkat Azimov, Vladislav Petukhov and Abdulkholik Lakaev*

Acoustic Emission based Crack Tracking for Concrete Structures

*Fengqiao Zhang\*a, Yuguang Yang*

# Proceedings of ICAE9

## Contents

36-S001 Damage Detection Through Fretting Emission in Center-Hole CFRP Skin of Cantilever Wing Box Under Constant-Moment Fatigue Loading, *Ryan J Neel, Jonathan Awerbuch, Tein-Min Tan, Didem Ozevin*

36-S009 Damage Detection Through Acoustic Emission During Post-Fatigue Residual Strength Test of CFRP Skin of a Cantilevered Wingbox Under Constant-Moment Loading  
*Ryan N Neel, Jonathan Awerbuch, Tein-Min Tan, Didem Ozevin*

36-S017 Development of damage detection method in type-III hydrogen pressure vessel by acoustic emission  
*Takuma Matsuo, Hiroki Orito, Kotaro Hase*

36-S023 Noise Tolerant and Wireless AE Measurement System for Process Monitoring  
*Kaita Ito, Kazuki Takahashi, Manabu Enoki*

36-S027 Sensing and statistical analysis of acoustic emission due to crack rubbing/clapping in thin sheet metals  
*Roshan Joseph, Victor Giurgiutiu*

36-S037 Progress in Sensitivity Verification of AE Sensors  
*Kanji Ono*

36-S043 Transmitters for the face-to-face sensor sensitivity verification - is their scatter tolerable?  
*Hartmut Vallen*

36-S051 Monitoring Fracture Formation in Additively Manufactured Anisotropic Rocks  
*Liyang Jiang, Hongkyu Yoon, Antonio Bobet, Laura J. Pyrak-Nolte*

36-S056 Tensile Test of 3D Printed Specimens for Demonstrating the Performance of Acoustic Emission Measurement Systems, *Hironobu Yuki, Tomona Murata*

36-S061 Evaluation of Damage Depth Inside Concrete Using Surface Wave Tomography  
*Norihiro Ogura, Tomoki Shiotani*

36-S067 Internal damage detection of RC bridge decks with uniformly distributed elastic wave sources  
*Hidefumi Takamine, Yuki Ueda, Kazuo Watabe, Katsufumi Hashimoto, Tomoki Shiotani*

36-S073 Monitoring geochemically-induced fractures in synthetic rocks  
*Chven A. Mitchell, Laura J. Pyrak-Nolte*

36-S079 Omnidirectional horizontal shear acoustic emission sensor for improved location analysis  
*Jason Philtron, Cody Borigo, Steven Owens, Ronnie K. Miller, Joseph L. Rose*

36-S085 Characterization of fiber break by quantitative acoustic emission in a model composite carbon/epoxy  
*Zeina Hamam, Nathalie Godin, Claudio Fusco, Thomas Monnier*

36-S091 Damage identification in composite tubes through acoustic emission monitoring  
*Neha Chandarana, Emmanuel Ramasso, Constantinos Soutis, Matthieu Gresil*

36-S097 Overview of Acoustic Emission in Monitoring Powder Technology  
*Eric Serris, Ana Cameirao, Frederic Gruy, Jean-Michel Herri, Gerard Thomas*

36-S103 AE measurement during friction stir welding of flame-resistant magnesium alloy with simulated inclusions  
*Kazuki Takahashi, Takayuki Shiraiwa, Manabu Enoki, Kaita Ito, Eitaro Yukutake*

36-S107 Structural Health Monitoring of Mooring Chains Crack Initiation and Growth using Acoustic Emission  
*Angela Angulo, Slim Soua, Tat-Hean Gan*

36-S112 Characterization of Microdamage of Flexible Solar Cell under Fatigue Load using AE and LT Techniques  
Takahiro Matsueda, Shuichi Wakayama, Kosuke Nakahara, Akihiro Takano

36-S118 Acoustic Emission Measurements of Detensioning and Transport of Prestressed Reinforced Concrete Bridge Girders, Dryver Huston, Robert Worley II, Mandar Dewoolkar, Tian Xia, Daniel Orfeo

36-S124 Application of Non-Contact Laser Impact with AE Analysis and Tomography Technique for Damage Identification in Concrete, *Tomoki Shiotani, Katsufumi Hashimoto, Masaharu Nishikino, Katsuhiro Mikami*

36-S130 Damage Quantification of RC decks by Means of Rain-Induced AE Excitations and Source Location Bias  
Katsufumi Hashimoto, Tomoki Shiotani, Kazuo Watabe, Hidefumi Takamine

## 36-S136 Development of prestressed concrete bridge tendon damage diagnosis system using acoustic emission technique

36-S142 Development of Structural Health Monitoring Technology for Internal Tendon of PSC Bridge Using Acoustic Emission Technology. *Dong-Hyun Kim, Yoon-Gi Hong, Dong-Woo Seo, Ki-Tae Park*

36-S148 Use of Acoustic Emission for identifying Gas-Liquid mixing regime in agitated vessel applying machine learning

## 36-S154 Acoustic Emission in Process of Thermal Decomposition of Potassium Hydrogen Carbonate Crystals.

36-S159 Acoustic Emission based Crack Tracking for Concrete Structures

Jingqiao Zhang, Faguang Yang

**Post-Conference Submission – non-peer reviewed**  
36-S165 A new time-domain feature (RKM) for Acoustic Emission transient signal processing

36-S172 Omnidirectional shear acoustic emission sensor for improved location analysis

# **Damage Detection Through Fretting Emission in Center-Hole CFRP Skin of Cantilever Wing Box Under Constant-Moment Fatigue Loading**

Ryan J. Neel<sup>1</sup>, Jonathan Awerbuch<sup>1</sup>, Tein-Min Tan<sup>1</sup>, Didem Ozevin<sup>2</sup>

<sup>1</sup> Drexel University, Philadelphia, PA 19104, USA

<sup>2</sup> University of Illinois at Chicago, Chicago, IL 60607, USA

## **I. ABSTRACT**

This study addresses the effect of damage accumulated during fatigue loading of a carbon-fiber reinforced polymer (CFRP) panel on acoustic emission (AE) waveforms. A 610-mm by 1,067-mm, 18-ply, nearly quasi-isotropic CFRP panel containing a 79-mm diameter hole at its center was attached as a top-side component (e.g., skin) of a cantilevered wing box structure subjected to constant-moment fatigue loading. The fatigue loading consisted of three 55,000-cycle test segments, sequentially increasing the maximum load, at a constant R-ratio of 0.1 and at a load frequency of 0.375 Hz. The fatigue test was interrupted periodically to conduct quasi-static loading/unloading to assess strain redistribution via digital image correlation (DIC). AE was monitored throughout the test sequence, using six R15I sensors, installed concentric to the central hole at a 406 mm diameter, equally spaced. Flash thermography and pulse echo and phased array ultrasonic inspections were used to intermittently assess the state-of-damage in the vicinity of the hole. Special attention was given to identify the emission generated by fretting among the newly formed delaminated surfaces. It is shown that fretting emission is dominant during cyclic loading of large composite panels and it can be used to pinpoint existing damage.

## **II. INTRODUCTION**

The overwhelming majority of studies on acoustic emission (AE) in composites has been conducted on small-scale specimens such as tensile coupons, three- and four-point bending, or mode-I and mode-II cantilever beam type testing under quasi-static loading conditions. Major effort has been directed toward identifying failure mechanisms during loading, comparing AE-signal features with post-mortem fracture surface morphologies as observed via microscopy.

These studies are, however, of limited utility when testing large composite structures that are subjected to complex loading functions under realistic loading rates. In such cases, voluminous AE-signals are generated nearly simultaneously from multiple sites at rapid rates. It should be expected that in large composite structures a significant amount of AE activity is caused by fretting among existing fracture surfaces (e.g., non-visual impact damage, disbonds, and manufacturing anomalies) and by newly formed fracture surfaces that normally occur during loading (e.g., delamination, fiber/matrix interfaces during fiber pullouts, matrix splitting, etc.). While a new crack extension generates emission only once, at the instance of its occurrence, the subsequent emission resulting from the fretting between the newly formed fracture surfaces could continue for extended segments of loading. Realizing that the number of fracture surfaces in composite structures is indeed extremely large, it should be expected that the fretting generated emission (FGE) exceeds by far the damage generated emission (DGE).

It was shown in [1,2] that damage progression could be tracked under quasi-static loading by accounting for only the high amplitude/high energy AE-signals by considering only AE-signals which hit a large number of sensors. The authors concluded that locating the site of damage and tracking its progression in large composite structures using the commercially available location algorithms is sufficiently accurate. On the other hand, it was shown in [3] that by subjecting a coupon to cyclic loading the resulting localized FGE aided in locating non-visual impact damage. Similarly, the FGE was used to track progression of delamination [4].

While it is difficult to overcome the many difficulties and ambiguities associated with monitoring AE in composite structures during fatigue, it is important to determine to what extent the available

commercial AE instrumentation could be relied upon for the purposes of detecting, locating and tracking damage progression in large composite structures.

### III. EXPERIMENTAL PROCEDURE

The experimental work was conducted using the Airframe Beam Structural Test (ABST) fixture, Figure 1, operated by the Structures and Materials Laboratory at the FAA William J. Hughes Technical Center in Atlantic City International Airport, NJ. The four 222-kN hydraulic actuators are synchronized to render constant moment, torsion, horizontal shear and vertical shear loading. A detailed description of the ABST fixture and its different supporting systems is provided in [5].

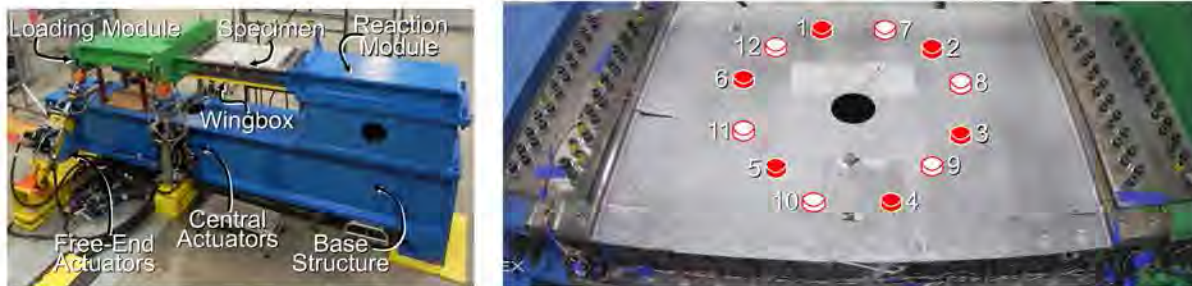


Figure 1. General view of the Airframe Beam Structural Test (ABST) fixture [5].

Figure 2. General view of the test panel instrumented with 6 WDI (no. 1-6) and 6 R15I (no. 7-12) sensors.

The test panel, attached at the top-side of the wing box, was a 610-mm wide, 1,067-mm long, 18-ply (3.56-mm) thick, nearly quasi-isotropic carbon fiber reinforced plastic (CFRP) panel with a through-the-thickness 79 mm diameter hole at its center, Figure 2. The panel was placed with the 0° plies positioned along the length of the panel. The details of the panel attachment are described in [5].

By applying constant moment loading to the wingbox, the panel was subjected to constant amplitude, sinusoidal, cyclic loading, at a nominal frequency of 0.375 Hz and at R-ratio of 0.1. The test procedure constituted of three loading phases, each 55,000 cycles long, increasing the maximum load amplitude following each loading phase. The maximum loads applied during Phases A and B are 61% and 81% of the maximum load applied in Phase C, respectively.

The panel was continuously monitored via multiple still and video high magnification camera systems. The cyclic loading was interrupted every 10,000 cycles for deformation measurements (using strain gages and digital image correlation) and non-destructive inspections (NDI) of the state-of-damage using Flash Thermography, Phased Array and Pulse-Echo Ultrasonics [5].

All NDIs revealed that most of the damage appeared in the form of local delamination extending away from the fwd and aft sides of the open hole, Figure 3. Detailed results and discussion on the extent of the state-of-damage during the cyclic loading is provided in [5].

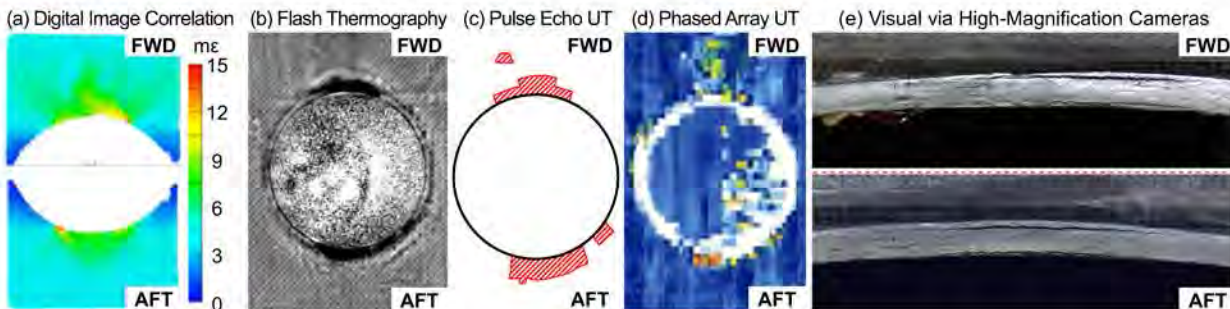


Figure 3. Damage revealed at the fwd and aft sides of the open hole at 165,000 cycle, different NDI methods and posttest visual of said regions.

The entire 16-channel AE system (including data acquisition boards, software (AEWin and Noesus), sensors and pre-amplifiers) was manufactured by Mistras Group, formerly known as Physical Acoustics Corporation (PAC). Six WDI and six R15I sensors were installed concentrically to the central hole, equally spaced ( $30^\circ$  apart) at a diameter of nominally 406 mm, Figure 2. Wave velocity calibration yielded wave velocities of 5,782, 4,795, and 4,484 m/sec along the  $45^\circ$ ,  $0^\circ$  and  $90^\circ$  direction, respectively. Noting that the  $45^\circ/90^\circ/0^\circ$  ply ratio of the laminate is 6/2/2, respectively, an average wave velocity of 5,207 m/sec was used. In this study only the results recorded with the R15I sensors are discussed.

#### IV. RESULTS AND DISCUSSION

**a. Acoustic Emission During Initial Quasi-Static Loading:** Prior to the start of each phase of the cyclic loading, the panel was subjected to several quasi-static loading/unloading cycles. Prior to Phase A, the panel was loaded twice to 50% and three times to 75% of maximum Phase A fatigue loading. The emission recorded by the six sensors during the first 75% load cycle is shown in Figure 4, accompanied by six selected AE-signal waveforms (one for each of the R15I sensors) and their corresponding frequency spectra.

As expected, most of the emission occurred in the first quasi-static load cycle, decreasing gradually in the subsequent load cycles (not shown here), which is mostly of low amplitude (<60dB). Most of the high amplitude (>75 dB) emission was generated at elevated loads during the first load cycle. With a few exceptions, no such high amplitude emission occurred in the subsequent quasi-static loading cycles. Several waveform clearly indicate the occurrence of multiple AE-signals. Such 'trains' of AE-signals might be also included in the other waveforms, as may be concluded from the corresponding multiple peak frequencies.

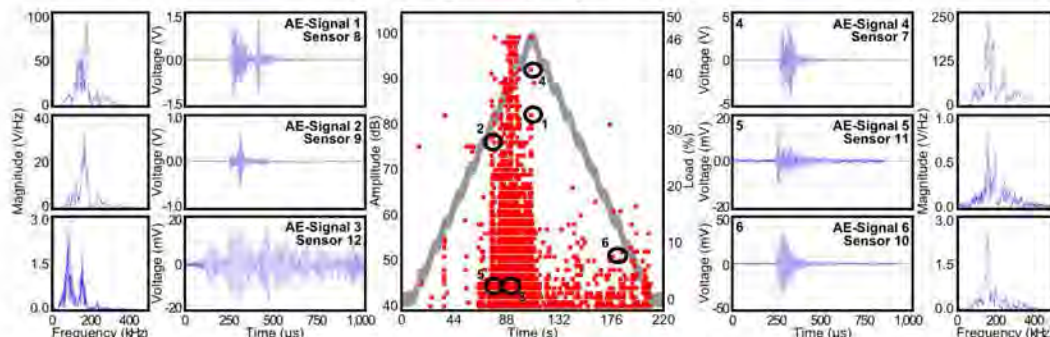


Figure 4. Emission recorded during pre-fatigue quasi-static loading/unloading (note the different scales).

Low amplitude emission occurs also during unloading, at low load levels. This low load - low amplitude emission is most probably due to fretting among the delaminated fracture surfaces, which emanated from the edges of the hole. It is expected that such fretting emission occurs during crack closure. The percentage of this emission of the total emission increases with load cycle. The burst-like AE-signal waveforms seen during unloading, at low load levels, one may speculate that this may have been caused by colliding surfaces during crack closure (e.g., buckling of pulled-out fibers and matrix lacerations).

**b. Acoustic Emission During Cyclic Loading:** A large amount of emission was recorded during the test. The total number of AE hits, recorded by the 12 sensors during the quasi static and the three 55,000-cycle loading phases, exceeded one million, all filed (for ease of post-test analyses) in approximately 9,800 files, automatically generated, each 100 MB to 200 MB in size, for a total of nearly 1 TB size storage. These files include all the standard waveform information as well as complete, 2 millisecond-long, waveforms, as provided by AEWin software package (V.E.3.5.2). For brevity, only selected results recorded during a brief, representative, 100-cycle segment of Phase 'C' of the test (130,025 to 130,125 cycles) are discussed herein.

The different channels recorded different AE activities in terms of hits rate and their occurrence throughout the load range, Figure 5. These differences are attributed primarily to sensor placement relative to the fatigued-damaged region, which occurred primarily in the aft and fwd sides of the open hole (as marked in Figure 2). The constant hit rate (of approximately 280 hits per cycle) implies repeated fretting among existing delaminated surfaces, with little if any new damage forming during this particular 100-cycle loading segment. The three-dimensional plots show that emission was generated repeatedly at the same load level, either during loading or unloading, including at very low loads.

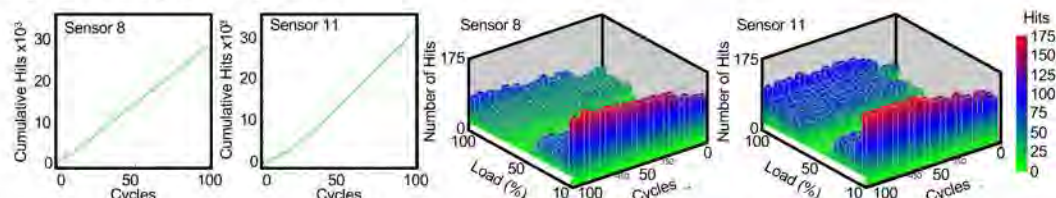


Figure 5. Number of acoustic emission hits recorded by two arbitrarily selected sensors during a 100-cycle test segment of Phase 'C' of the test (130,025 to 130,125 cycles), and the corresponding three-dimensional plots showing that a significant number of emission occurred at low load levels throughout this cyclic load segment, indicating fretting-generated emission.

The repeatability of the hits at the same load level, during both loading and unloading, is clearly seen in the arbitrarily selected two-cycle load segment shown in Figure 6. Identical pattern was recorded throughout this loading segment. The waveforms of six selected AE-signals, and the corresponding frequency spectra all indicate 'noise'-like waveforms, occurring at both loading and unloading, including at load as high as 90% of peak loads. The AE-signals generated at the same load level during the two consecutive load cycle, generated either during loading or unloading (e.g., pairs 1 &11, 3 & 9, and 7 &12), are strikingly similar, as are their corresponding frequency spectra. This repeated pattern is a result of the repeated fretting between neighboring fracture surfaces as they come in contact (and may also intermittently brush against each other) during the load cycle. The pick frequencies of these waveforms (and all others not shown here) range between 138 to 157 kHz, with second peak occurring at approximately 100 kHz, as expected considering the frequency response of R15I sensors.

Little if any emission occurred at peak loads, marked by the dashed vertical lines in Figure 6. No emission occurred above 85% of peak load. A few high amplitude hits (> 80 dB) occurred in the range of 70%-80% of peak load. Most of the emission is of low amplitude (<50dB), with a few hits of mid-range amplitude (60-70 dB). It could be concluded, therefore, that all this emission has been generated by fretting of existing fracture surfaces rather by the occurrence of new damage. The amplitude ranges of this fretting-generated emission is within the same range of the emission attributed to matrix cracks (40-60 dB), delamination (60-80 dB), and fiber breakage (>80 dB).

The waveforms shown in Figure 6 are not characteristic of the expected burst-like stress waves, typically generated by an abrupt crack extension. Several waveforms shown in the figures are of very low amplitude, just above the 40 dB threshold (marked by the two horizontal lines) while other waveforms are of amplitude as high as 60-70 dB. That is, fretting could generate also medium to high amplitude AE-signals. All waveforms shown in the figure constitute a cluster of several overlapping AE-signals, which are considered by the AE system as single hits with extended duration, energy and exceptionally long rise time. The duration of such a 'train' of AE-signals depend on the particular selection of the HDT and HLT (which were 600  $\mu$ sec and 1,200  $\mu$ sec in this test, respectively). Therefore, key AE features like amplitude, energy, duration, counts, risetime, etc., are not necessarily indicative of any particular mode of damage.

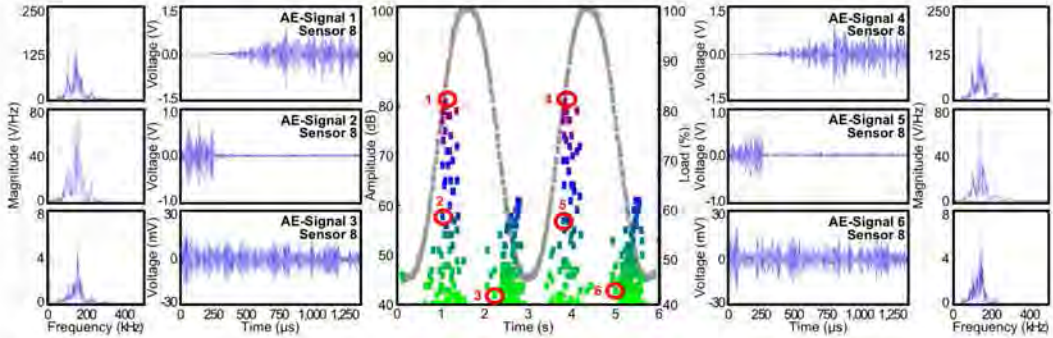


Figure 6. Emission recorded during arbitrarily selected two-cycle segment during Phase 'C' of the fatigue test (starting at cycle no. 132,101), showing emission generated repeatedly at the same low load levels during both loading and unloading of the load cycle.

These AE-signal indicate that no new damage occurred during the aforementioned brief 100-cycle test segment. It seems that merely considering the emission generated near the peak load (accomplished either by real time or posttest filtering of emission generated below prescribed, often arbitrarily, load level) as generated only by newly formed damage could yield misleading conclusions.

Amplitude distribution histograms (ADH) and absolute energy distribution histograms (EDH) of hits recorded by a selected sensor are plotted in Figure 7 for the 100-cycle segment. Nearly identical distributions were recorded by the other five AE channels. The plots show that most hits are of an amplitude range of 40-60dB. A relatively smaller number of hits are of higher amplitude range, up to 82dB, occurring throughout the 100-cycle segment.

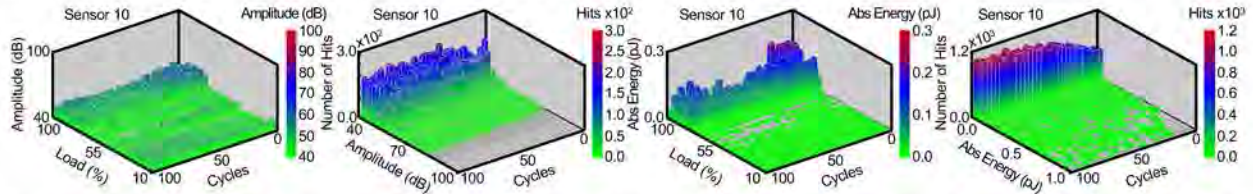


Figure 7. Amplitude and energy distribution histograms of hits recorded by a single sensor during a 100-cycle segment, showing fretting generated emission having amplitude range of 40-55dB while most hits' are of negligible absolute energy.

The EDHs show very low absolute energy, with most hits being of 'zero' energy, typical when "noise" triggers the AE sensors. Most of this so-called noise was generated by the fretting among the delaminated fracture surfaces in the fwd and aft sides of the open hole. Nearly identical ADHs and EDHs were recorded by the first AE-signal hit of three-, four-, and five-hit events, captured by any random combination of sensors, Figures 8-10.

**c. Planar Location of Acoustic Emission Events During Cyclic Loading:** By using the built-in localization algorithm provided by the AEWIN software, the fretting-generated emission, caused by the local delamination in the vicinity of the aft and fwd sides of the open hole, could be located in real time. For this purpose, all six-sensor configurations were tested to determine the accuracy of localizing the fwd and aft damaged zones considering: any three-, four, five-, and six-hit events and all combinations of three-, four-, and five- hit events recorded correspondingly by three, four or five neighboring sensors. Data were filtered based on different amplitude and absolute energy ranges, corresponding with new damage and fretting.

In most cases the correlation between the AE localization and actual damage was quite poor, Figure 11a. When localization is based on four neighboring AE sensors, and considering only low amplitude (45-50 dB) and low absolute energy (0-100) first hit AE-signal (i.e., those events which most certainly were generated by fretting only) an excellent correlation between the actual

(Figure 3) and the detected damage in the aft side of the open hole is seen, Figure 11b and Figure 11c, respectively. Of the 78 and 88 four hits events, all but 7 and 7 events are near the open hole, respectively.

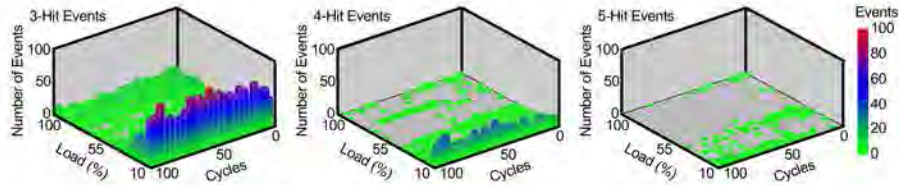


Figure 8. Events distribution histograms of three-, four-, and five-hit events during a 100-cycle segment, showing that high strength AE-signals (i.e., 5-hit events) occurring at low load levels.

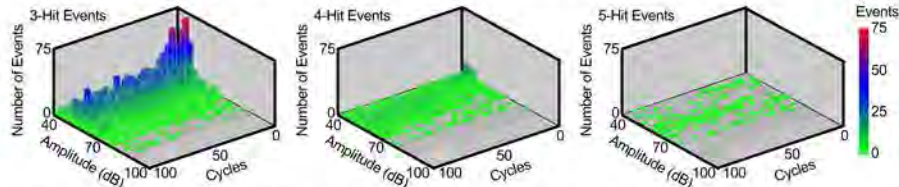


Figure 9. Amplitude distribution histograms of the first hit of three-, four-, and five-hit events during a 100-cycle segment, showing that fretting generated AE-signals could hit multiple sensors.

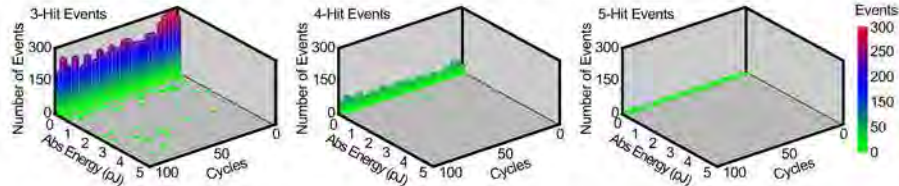


Figure 10. Absolute energy distribution histograms of the first hit of three-, four-, and five-hit events during a 100-cycle segment, showing that fretting generated AE-signals could hit multiple sensors, all of negligible absolute energy while being recorded as being of low and medium amplitude and of long duration.

The presence of a large discontinuity (e.g., an open hole), the nearly simultaneous emission generated by fretting from multiple sites in the panel, the highly directional-dependent wave speed in the material, and the expanding new damage in the vicinity of the hole (i.e., primarily delamination) make planar localization of damage in large composite panels highly inaccurate. Further, the location of the primary damage (at the aft and fwd sides of the open hole) relative to the surrounding recording AE sensors causes significant errors since the damage occurred mostly outside the sensors' polygon, e.g., Figure 11a. In other words, implementing localization requires a targeted approach, which must depend on the particular circumstances of the testing.

Further, the localization of damage in composite subjected to fatigue loading is fraught with difficulties because of the propensity of multiple sources to generate AE signals within a time interval shorter than the source-sensor travel time. In such cases, the AE system may consider these multiple sources to be generated by a single source which is located arbitrarily, i.e., mislocated. The probability for this to occur during cyclic loading of large composite structures could be quite high, depending on the presence of the particular state-of-damage and the many material and testing variables such as wave propagation characteristics, loading frequency, AE instrumentation set up, sources-sensors distances, etc.

**d. A Further Discussion on Distinguishing Fretting Emission:** As discussed earlier, the AE burst-like waveforms recorded during quasi static loading were clearly generated by new damage, Figure 4. On the other hand, the AE-signals waveforms recorded during the cyclic loading seems to be generated by 'noise', i.e., they were mostly due to fretting, Figure 5. In order to distinguish more readily the damage generated emission from that generated by fretting the Principal Component Analysis (PCA) approach was examined.

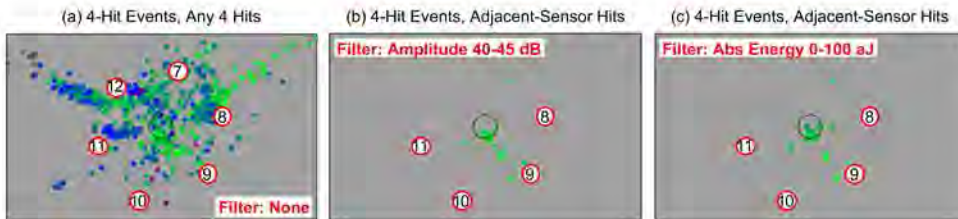


Figure 11. Planar location scatter plots of four- hit events, recorded by: a) any four sensors; b) four specified sensors (as indicated) considering only first hits of 40-45 dB amplitude; and c) same four sensors considering only first hits of 0-100 AJ absolute energy.

Principal Component Analysis provides opportunities to assess trends in large data sets that may otherwise be obscured by the large quantity of data or large dimensionality of the data set. To test this hypothesis, a combined dataset was constructed in Noesis for the purpose of conducting PCA. The combined data set included: 1) AE activity recorded during the first quasi-static strain survey up to 75% of the maximum Phase 'A' fatigue loads (Figure 4); and 2) AE activity recorded during a 100-cycle segment of fatigue during Phase 'C' (Figure 6). The clustering algorithm and all pre-processing activities were carried out in the Noesis software, using all waveform features except threshold and parametric. Subsequently, the data set was normalized via zero mean and unit variance methodologies, respectively. Finally, PCA was conducted and 2D plots of principal components were constructed.

The two primary principle components (PC-0 and PC-1) are plotted in Figure 12 for all AE-signals generated during the first quasi static loading/unloading cycle (see Figure 4) and during the 100-cycle fatigue load segment. All but 18 of the 2,471 AE-signals generated during the quasi-static loading/unloading cycle (Figure 12a) are embedded in the cluster of 122,650 AE-signals generated

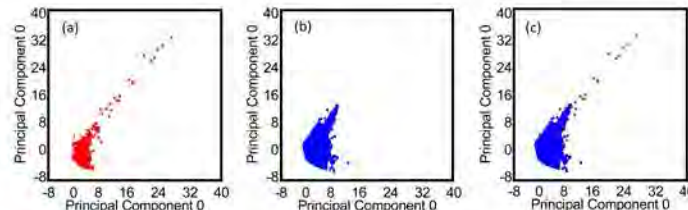


Figure 12. Principle component analyses (PCA0 vs. PCA1), comparing AE-signals recorded during the: a) first quasi static/unloading cycle; b) 100-cycle fatigue segment; and c) comparison of the two groups of AE-signals.

during the 100-cycle fatigue test segment (Figure 12b), thus, they were most probably also generated by fretting (Figure 12c). In other words, AE-signals presumably generated by damage overlap those generated by fretting. Further, all of the hits associated with the four-hit events located near the aft side of the open hole (Figure 11b and Figure 11c) are embedded in the fatigue-related cluster shown in Figure 12b. To further examine this hypothesis, the AE-signals generated, separately, during the first quasi-static loading and unloading segments were examined, Figures 13a and Figure 13b, respectively.

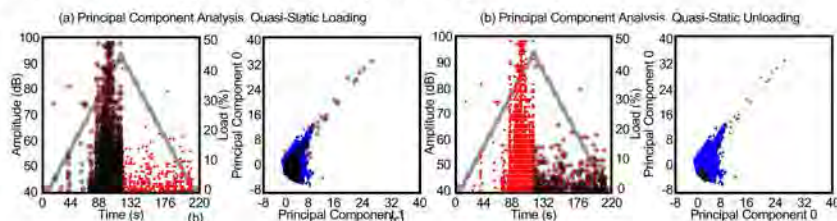


Figure 13. Principle component analyses (PCA0 vs. PCA1), comparing separately the AE-signals recorded during the loading and unloading segments of first quasi-static loading/unloading cycle (black clusters) with the 100-cycle fatigue segment (blue clusters).

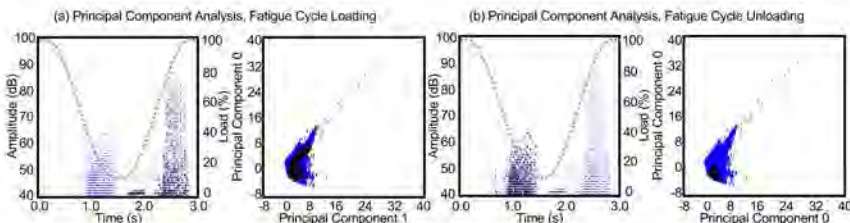


Figure 14. Principal component analyses (PCA0 vs. PCA1), showing the AE-signals recorded during the loading and unloading segments of cycle 132,025 (black clusters) together with the AE-signals recorded during both the 100-cycle fatigue segment (blue cluster) and the first quasi-static loading/unloading (red cluster) shown in Figure 12.

These AE-signals are embedded (darker regions) in the clusters generated during the 100-cycle fatigue load segment, respectively, clearly indicating that fretting emission occurs during both quasi-static loading and unloading. For further confirmation, same analysis was conducted for a single cyclic loading/unloading, Figure 14. The resulting PC-0 vs. PC-1 plots for the loading and unloading phases of this fatigue load cycle are nearly identical to those plotted for the first quasi-static loading and unloading, confirming that significant emission occurs also during a quasi-static loading of a pristine composite panel.

## V. CONCLUSION

During the 100-cycle test segment, no damage was observed. This was based on the analyses of individual waveforms, low amplitude AE signals at the peak loads and significant overlaps of PCAs during loading and unloading segments. On the other hand, the localization result of low amplitude signals generated due to existing damage surfaces agreed very well with DIC and flash thermography images. It is concluded that the periodic analyses of fretting emissions can be used to pinpoint the existing damage instead of identifying individual damage emissions.

## VI. ACKNOWLEDGMENT

This study was conducted in support of the Cooperative Research and Development Agreement (CRDA) between the Federal Aviation Administration in Atlantic City, New Jersey, and The Boeing Company (Boeing Research & Technology) on bonded repair size limit, with the participation of Drexel University. Drexel was partially supported by a grant from the FAA (grant number 15-G-017). The authors wish to acknowledge the support of John G. Bakuckas, Jr., of the FAA William J. Hughes Technical Center, for facilitating this study and especially note the work of Reewanshu Chadha, of Diakon Solutions, for conducting the mechanical testing program.

## VII. REFERENCES

1. Frank A Leone Jr, Didem Ozevin, Jonathan Awerbuch, and Tein-Min Tan, "Detecting and Locating Damage Initiation and Progression in Full-Scale Sandwich Composite Fuselage Panels Using Acoustic Emission," Journal of Composite Materials, June 2013 vol.47, no. 13, pp. 1643 – 1664.
2. Amey Khanolkar, Andrew Bergan, Didem Ozevin, Jonathan Awerbuch, and Tein-Min Tan, "Acoustic Emission Testing of a Curved Pultruded Rod Stitched Efficient Unitized Structure (PRSEUS) Under Combined Loading," Proceedings of the American Society of Composites 27th Annual Technical Conference, Arlington, TX, October 1-3, 2012.
3. Ghaffari S and Awerbuch J., Monitoring acoustic emission in impact-damaged composites. In: Proceedings of the second international symposium on acoustic emission from reinforced composites. Montreal, July, 1986, pp. 121–125.
4. Cohen J and Awerbuch J. Monitoring delamination progression in composites through acoustic emission during fatigue loading. In: Proceedings of the fourth Japan-US conference on composite materials. Washington, DC, June, 1988, pp.1035–1046
5. John G. Bakuckas, Jr., Reewanshu Chadha, Paul Swindell, Michael Fleming, John Z. Lin, J.B Ihn, Nihar Desai, Mark Freisthler, Ryan J. Neel, Jonathan Awerbuch and Tein-Min Tan, "Assessment of Bonded Repairs of Composite Wing Panel Structure," 36th Conference & 30th Symposium of the International Committee on Aeronautical Fatigue and Structural Integrity, Krakow, Poland, June 2-7, 2019.

# **Damage Detection Through Acoustic Emission During Post-Fatigue Residual Strength Test of CFRP Skin of a Cantilevered Wingbox Under Constant-Moment Loading**

Ryan J. Neel<sup>1</sup>, Jonathan Awerbuch<sup>1</sup>, Tein-Min Tan<sup>1</sup>, Didem Ozevin<sup>2</sup>

<sup>1</sup> Drexel University, Philadelphia, PA 19104, USA

<sup>2</sup> University of Illinois at Chicago, Chicago, IL 60607, USA

## **I. ABSTRACT**

Post-fatigue residual strength testing of carbon-fiber reinforced polymer (CFRP) panels is typically conducted to characterize the effect of the state-of damage on residual strength. It is expected that acoustic emission (AE) characteristics are quite different in fatigue-damaged CFRP laminates, as compared with pristine specimens. This study focuses on the effect of the internal damage accumulated during fatigue on the characteristics of AE generated during post-fatigue residual test loading. This test was conducted on the same panel described in the accompanying paper under the same AE test conditions. The CFRP panel was attached as a top-side component (e.g., skin) of a cantilevered wing box structure. The assembly was subjected to twelve quasi-static constant-moment loading/unloading cycles, sequentially increasing the load until panel fracture. Acoustic emission was monitored during loading using six R15I sensors. Far-field and near-field digital image correlation (DIC) systems were used to monitor local and global strain fields. Visual, flash thermography, and phased array ultrasonic inspections were used to assess the state-of-damage in the vicinity of the hole. In general, results revealed good correlation between AE activity and regions of primary damage and imminent fracture could be anticipated based on a combined, four-prong, approach based on information provided by the AE, namely: i) emission accumulation rate; ii) intensity of the AE signals; iii) planar location of the AE sources, and iv) emission distinguished via Principal Component Analysis.

## **II. INTRODUCTION**

Studies on monitoring acoustic emission (AE) in composites are typically performed by testing small scale pristine specimens under quasi-static loading conditions. Composite-made aircraft structures, however, are large in size and are normally subjected to high-cycle fatigue loading. The resulting fatigue damage accumulates during service, often initiating at weakened sites, such as locations of non-visual impact damage, disbonds, manufacturing anomalies, or local (patch or scarf) repairs. Therefore, monitoring AE during post-fatigue loading (i.e., of fatigue-damaged composite-made structures) could aid in assessing the state-of-damage.

Invariably, delamination is a primary mode of such damage, which extends during service. The exposed delaminated fracture surface often reveals, under microscopy, also broken fibers, fiber/matrix interfacial failures, and matrix microcracking. Therefore, when studying fatigue behavior of composites, a great deal of attention is also given to post-fatigue residual strength of the component, which is determined by conducting quasi-static loading to fracture.

The size and shape of the delaminated region is examined via a variety of non-destructive inspection (NDI) techniques such as ultrasonics, radiography, and thermography. During residual strength testing such NDIs normally require pause, or interruption, in loading. Monitoring AE during post-fatigue residual strength test could provide real time indication on: a) the presence of existing damage; b) new damage initiation load; c) rate of damage progression; d) localizing existing and new damage; e) tracking damage progression; and f) anticipating fracture load and site.

Real-time detection of damage initiation load of pristine composite structures via AE is the most readily available approach. This assumes, however, that AE is generated solely by new damage.

For non-pristine structures, existing damage (e.g., caused during fatigue) may generate early fretting emission, i.e., at low loads, which is unrelated to new damage. In other words, early AE initiation load may indicate the presence of existing damage. To avoid misguided assumptions, the distinction of fretting-generated emission (FGE) from damage-generated emission (DGE) needs to receive primary attention. This could be accomplished by targeted waveform analyses of the AE signals. Rate of damage progression is associated with increasing rate of the corresponding AE-signals. Fracture load is normally anticipated by the increasing rate and intensity of emission. Source localization algorithms, readily available in the commercial AE instruments, provides means to locate new damage and track its progression.

This study focused on the applicability of AE to detect damage initiation, locate its site, track its progression and anticipate imminent fracture of a large composite panel that contains both a large discontinuity (i.e., an open hole) and existing damage caused by an extended fatigue loading.

### III. EXPERIMENTAL PROCEDURE

The experimental work was conducted at the Airframe Beam Structural Test (ABST) fixture, Figure 1, operated by the Structures and Materials Laboratory at the FAA William J. Hughes Technical Center in Atlantic City International Airport, NJ. The four hydraulic actuators are synchronized to render the desired loading function. A detailed description of the ABST fixture and its different supporting systems is provided in Bakuckas et al. [1].

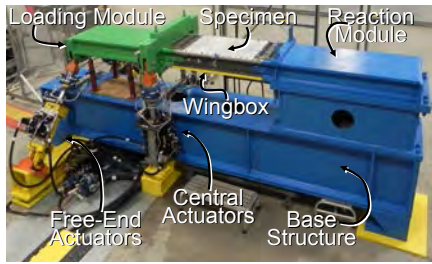


Figure 1. General view of the Airframe Beam Structural Test (ABST) fixture [1].

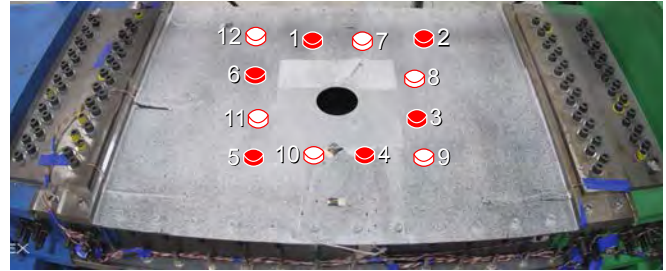


Figure 2. General view of the test panel instrumented with 6 WDI (no. 1-6) and 6 R15I (no. 7-12) sensors.

The test panel was a 610-mm wide, 1,067-mm long, having 18-ply (3.56 mm-thick), being nearly quasi-isotropic carbon fiber reinforced plastic (CFRP) panel with a through-the-thickness 79.4 mm diameter hole at its center, Figure 2. The panel was placed with the 0° plies positioned along the length of the panel. The details of the panel attachment are described in [1].

The panel was previously subjected to constant amplitude, sinusoidal, cyclic loading, under constant moment loading, at a frequency of 0.375 Hz and at R-ratio of 0.1, for 165,000 cycles, as described in [1]. Subsequently, and following post fatigue inspection, the panel was subjected to a residual strength (RS) test. The test included 12 quasi-static loading/unloading cycles, incrementally increasing the load up to failure, numbered RS-1 through RS-12. Sinusoidal load profile was applied, with the last loading (RS-12) at an approximate average loading rate of 11.1 kN/min and 15.7 kN/min of the inboard and outboard actuator pairs. Final loading was terminated prior to catastrophic fracture at 60.7 kN and 86.2 kN, respectively, to ensure that the panel remained intact upon removal from the ABST test fixture for post-test NDI. This paper discusses the AE recorded only during the last (RS-12) loading to failure.

The panel was continuously monitored via multiple still and video high magnification camera systems. Digital image correlation (DIC) was used to continuously monitor panel deformation. Strain was monitored throughout loading using strain gages at pre-selected sites. Additionally, non-destructive inspections (NDI) of the state-of-damage were conducted upon each unloading

using flash thermography (FT) and phased array (PA) ultrasonic. Results of all these measurements and inspections are discussed in [1].

A 16-channel AE system, manufactured by Mistras Group, formerly known as Physical Acoustics Corporation (PAC) was used in this program, including data acquisition boards, software (AEWin and Noesis), sensors and pre-amplifiers. Six WDI and six R15I sensors were installed around the central hole. The six R15I sensors were mounted concentric to the central hole,  $60^\circ$  apart: sensors no. 7, 8, 10, and 11 at a radius of 168 mm and sensors no. 9 and 12 at a radius of 240 mm, Figure 2. The six WDI sensors were displaced, as needed, for space considerations. Wave velocity calibration yielded wave velocities of 5,782, 4,795, and 4,484 m/sec along the  $45^\circ$ ,  $0^\circ$  and  $90^\circ$  direction, respectively. Noting that the  $45^\circ/90^\circ/0^\circ$  ply ratio of the laminate is 6/2/2, respectively, an average wave velocity of 5,207 m/sec was used. In this study only the results recorded with the R15I sensors are discussed.

#### IV. RESULTS AND DISCUSSION

Free-edge delamination is expected to be the dominant failure at the fwd and aft sides of the open hole, as was confirmed via visual observations and NDIs conducted at the end of the fatigue test (to be shown below). Numerous prior studies often revealed that the delaminated fracture surface contains a large number of broken fibers, fiber/matrix interfacial failures, and extensive matrix micro-cracking – all of which are sources of AE. This complex damage is further extended during post-fatigue residual strength test.

**a. Characteristics of AE-Signals:** The hit amplitude of the AE-signals recorded by all six R15I sensors are shown in Figure 3, together with selected waveforms and their corresponding frequency spectra. A large number of AE signals (13.4%) were recorded at load levels below the previous peak load (i.e., RS-11 test of 78.2 kN). The amplitude of these AE-signals were of 40-50 dB (80.9%), 50-70 dB (19.6%) and above 80 dB (0.1%) ranges, normally associated (in small-scale laboratory coupon testing) with matrix cracking, delamination, and fiber breaks, respectively.

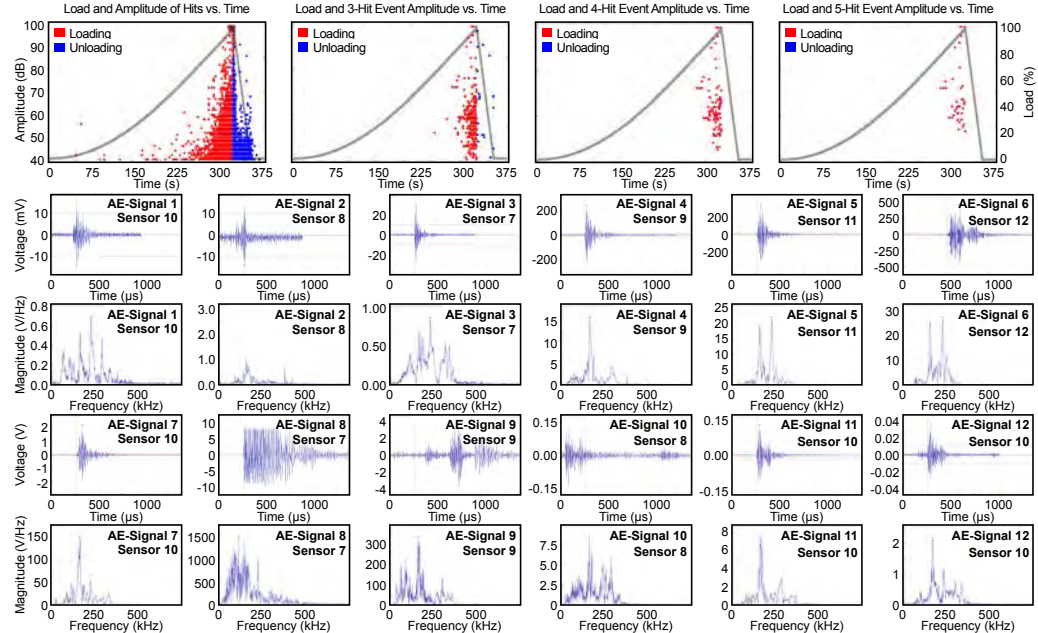


Figure 3. AE-signals recorded during the first post-fatigue RS loading, showing selected waveform at key load levels and their corresponding frequency spectra.

However, since no new damage is expected to occur at such low load levels, one may conclude that the majority of this emission resulted from fretting among the fracture surfaces formed during the prior extended fatigue test. Most of the low-load emission is of low amplitude (45 dB),

containing negligible energy, (e.g., AE-signals no. 1 and 2). Nearly all waveforms were generated by multiple AE-signals, i.e., 'trains' of hits (e.g., AE-signals no. 1, 2, 6 to 12), resulting in multiple peak and compounded frequency spectra, recorded by a 150 kHz resonance sensor. None of the low-intensity AE signals generated during the initial 65% of peak load (first 305 second in Figure 3) resulted in a locatable event (i.e., recorded by three or more sensors).

Further, sample AE-signals no. 3 and 10-12 where generated at relatively low load levels, during loading and unloading, respectively, when no new damage is expected. These representative AE-signals are similar to typical high amplitude burst-like AE-signals, normally associated with new damage. That is, it appears that fretting generates AE-signals are similar to those generated by matrix-dominated damage.

The propensity for train of hits to occur increases with load due to increasing rate of new damage (e.g., AE-signals no. 5 to 8). Similar, burst-like, AE signals were generated also during unloading, (e.g., AE-signals no. 9 to 12). The 7,636 AE-signals generated during loading to failure yielded 297 and 100 three- and four-hit locatable events, respectively. Figure 3 also indicates a significant increase in emission rate at approximately 80% of peak load. At that load the percentage of mid- and high- amplitude AE-signals increased rapidly. Nearly all this emission was generated from two distinct locations at the fwd and aft side of the open hole, as discussed below. Similar results were recorded for the prior post-fatigue quasi-static loading, to be reported elsewhere.

**b. Accumulation of AE-Signals:** The emission initiation load and the number and rate of AE-signals accumulated by the six sensors during the last residual strength test were quite different, depending upon their location relative to the damage progressing in the fwd and aft sides of the open hole, Figure 4. Since AE activity is affected by loading history (that is, by the previously formed and grown state-of-damage), it is not surprising that increased AE activity initiated at a relatively high load level, i.e., at 83% of peak load (or at 92% of the previous, RS-11, peak load), Figure 4a. Consequently, the subsequent AE accumulation rate is also relatively high. Sensors no. 7 and 10 registered the largest AE activity (70% of all AE signals recorded) due to their proximity to the fwd and aft damaged sites. That is, the increased AE activity recorded by a single sensor could aid in estimating the zonal location of extensive damage.

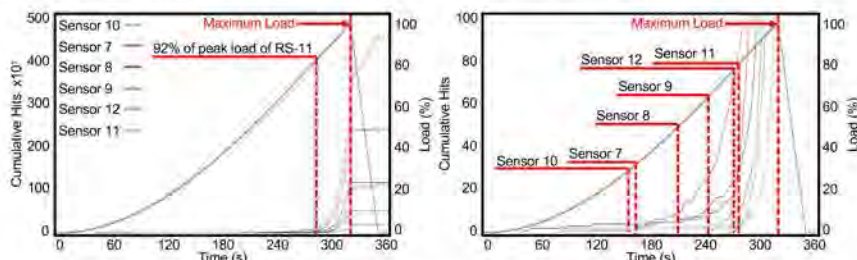


Figure 4. Emission recorded by all six AE channels during the final (RS-12) quasi-static loading to failure: a) full scale, showing increased AE activity in certain zones of the panel, notably AE-channels no. 7 and 10; and b) initial loading phase, showing emission initiation load and initial rate of emission accumulation at various locations of the CFRP panel.

Unloading was conducted by gradually decreasing the load (rather than loading to catastrophic fracture), following significant bursts of damage progression, which correspond with the high intensity AE signals near peak load, Figure 3. The two AE channels closest to the fwd and aft damaged zones recorded emission during unloading. Since the damage on the aft side was more extensive, channel 10 exhibited a higher AE activity, as expected. Channels no. 8, 11, and 12 registered no AE activity simply because the corresponding sensors separated from the panel during the sudden bursts of released energy during the final stages of damage progression.

The important aspect of determining emission initiation load could offer ambiguous results when considering individual sensors. As noted above, a large number of AE-signals hit fewer than three

sensors, i.e., less than 13.7% of the AE-signals ‘contributed’ to defining locatable events. Therefore, the initiation and accumulation of three- and four-hit events should be more relevant to monitoring damage initiation and accumulation in composite structures, as shown in Figure 5. The figure shows that either events initiated at or near the same load level. The change in slope coincide with unloading, as expected.

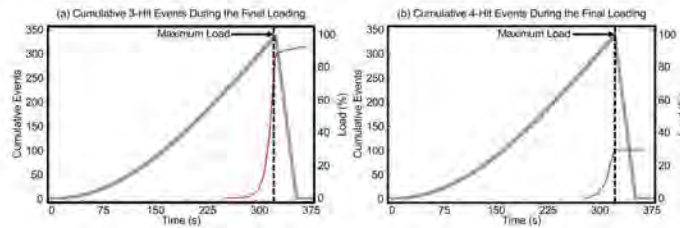


Figure 5. Initiation and accumulation of three- and four-hit events during final loading to failure, showing emission initiation load and accumulation rate prior to failure. Only a small fraction of the AE-signals took part in locatable events.

**c. Planar Location of Acoustic Emission Events During Residual Strength Testing:** Locating damage initiation sites and tracking their progression, in real time, are of particular importance in large composite-made fuselage panels, skins of aircraft wings and stabilizers and similar composite structures. Acoustic emission could serve this purpose, provided one is cognizant of the inherent and well-established inaccuracies and is satisfied with an approximate damage localization to aid in subsequent detailed inspection via other NDI methods. In this regard, the key issue is to determine the optimal AE data analyses procedures to accomplish that goal.

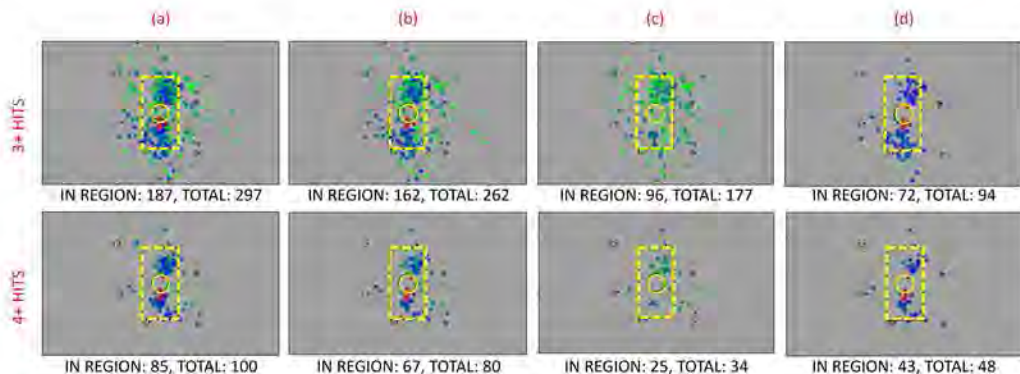


Figure 6. Planar localization scatter plots for any three-hit events generated during RS-12 loading, considering four scenarios: a) All events generated throughout the last RS loading; b) All events generated during the incremental loading from previous to the last RS loading; c) as in (b) for events having low first hit amplitude range (40-60 dB); and d) as in (b) for events having mid and high first hit amplitude range (60-100 dB).

Using the built-in localization algorithm provided by Noesis software, two-dimensional localization scatter plots, based on three- and four- hit locatable events, are shown in Figure 6. Two different data sets are shown in the figure: The events generated only during the loading phase, Figure 6a, show high concentration of events in the fwd and aft sides of the open hole: that is, 63% and 85% of three- and four-hit events, respectively, are within an arbitrarily selected 305x152-mm rectangle (with the 79.4 mm diameter hole at its center). Accounting only for the events generated during the final incremental load (from the previous peak load) yields only a slightly better correlation, Figure 6b.

Most of the first-hit low-amplitude AE-signals could not reach more than the three nearest sensors (i.e., they were mostly three-hit events), Figure 5c, either due to signal attenuation, the effect of the direction-dependent wave speed, wave dispersion, or due to the presence of existing damage in the path of the progressing AE-signal. Most of the mid- and high-amplitude events were

concentrated in the fwd and aft damaged regions, Figure 5d, with 77% and 90% of the three- and four- hit events, respectively, were located within said rectangle. That is, the multi-sensor/high-amplitude AE-signal offers the best planar localization of damage when using the built-in localization algorithm provided by the Noesis software, which confirms the results reported in [2,3].

The presence of a large discontinuity (e.g., open hole), combined with the particular site of the two damaged zones (i.e., open hole and the fwd and aft damage sites), render the otherwise desired redundancy of five- and six- sensor localization unhelpful. For example, 61 and 26 of the 297 three-hit events were four- and five- hit events, respectively, Figure 3. Additionally, the propensity that an AE source is located outside the triangle or rectangle formed by any three or any four sensor sets is quite high, potentially yielding inaccurate location of a large number of AE-signals. Further, the susceptibility that multiple damage (and fretting) sites emit nearly simultaneous AE-signals, i.e., within the short source-multi-sensor travel times, is highly realistic, rendering the AE system to consider such multiple AE-signals as a single source emanating from a misplaced, or arbitrary, location. Several of such scenarios were examined and confirm in this study, to be reported elsewhere.

The localization plots shown in Figure 6d are in general agreement with the images taken at peak load (Visual and DIC) or upon load removal (FT and PA), Figure 7. The damage emanating from the fwd and aft side of the open hole progressed in a slightly anti-symmetric fashioned, which can be also seen in the localization plots of Figure 6. The extended internal damage along the length of the panel, detected by phased array technique, was not captured by the localization plots. This is expected since damage in composites often extends abruptly, in intermittent and stepwise progressions, commencing near peak loads. While AE is effective in monitoring the evolution of such damage, often on the micro level (which is normally the precursor of the extended damage), the sudden, rapid, and extended damage generates a swift avalanche of AE-signals which are considered by the AE recording system as a few 'trains' of AE-signals, e.g., AE-signals no. 5 to 12 in Figure 3.

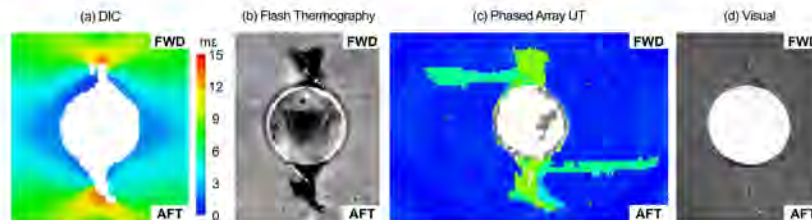


Figure 7. State of damage in the fwd and aft side of the open hole is seen visually, DIC, FT and PA. The DIC image was taken at peak load while the other images were recorded after load removal.

**d) About 'Trains' of AE-signals:** One of the inherent difficulties in monitoring AE in large composite structures is the rapid occurrence of multiple modes of damages emanating from different sites, often nearly simultaneously. In fact, this is the "Achilles heel" of monitoring AE in composites: many of the AE-signals contain overlapping waveforms, Figure 3.

In the representative cases shown Figure 3, as well as in most of the hundreds of AE-signals reviewed herein, the waveform indicates the occurrence of 'trains' of AE-signals. In all these cases the corresponding frequency spectra are highly compounded and contain multiple frequency peaks, i.e., they become 'noisier'. In fact, windowed FFT of the complete AE-signals indicates different frequency spectra for each individual waveform in the combined AE-signal, as shown in Figure 8 for AE-signal no. 9 depicted from Figure 3.

Since the review of the 7,636 AE-signals recorded during this loading is impractical, the distinction and separation of 'trains' of AE-signals may be possible by identifying a new, widowed FFT-based AE feature in order to bypass the need of reviewing each individual waveform.

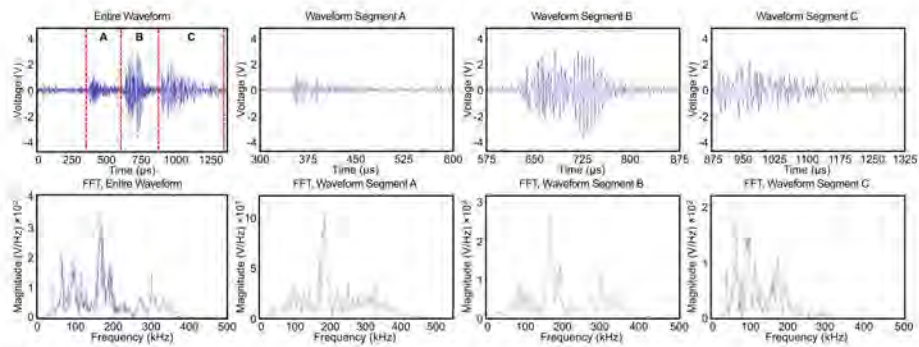


Figure 8. Analyzing AE-signal no. 3 of Figure 4: a) the complete waveform, indicating three different AE-signals; b) the corresponding frequency spectrum of the complete waveform of (a); c) windowed frequency spectrum for the first segment of the waveform (500-1000 $\mu$ s); d) windowed frequency spectrum for the first segment of the waveform (2000-2500 $\mu$ s); and e) windowed frequency spectrum for the first segment of the waveform (3500-4000 $\mu$ s).

**e. A Further Discussion on Determining Imminent Component Fracture Through AE:** It is well established that near peak load catastrophic damage in composites progresses abruptly, rapidly, and extensively. By its characteristic as a passive NDI, it should be possible to use the AE method as an early warning of imminent fracture and anticipating fracture site. The sudden increase in emission rate during RS-12 loading (Figure 3) and the high amplitude, burst-like, emissions recorded near and at peak load (e.g., AE signal no.8 in Figure 5) may provide prejudiced early warning. The Principal Component Analysis (PCA) approach was examined to determine whether it could provide another mean of distinguishing those AE-signals which might signify imminent fracture.

To test this hypothesis, the data set analyzed included the AE-signals recorded separately during loading and unloading. PCA and all pre-processing activities were carried out in the Noesis software, using all waveform features except threshold and parametric. Subsequently, the data set was normalized via the unit variance methodology. Finally, PCA was conducted and 2D plots of principal components were constructed.

The two primary principle components (PC-0 and PC-1) are plotted in Figure 9 for both sets of 7,636 and 2,302 AE-signals generated during loading and unloading, respectively, Figure 9a. Importantly, the two groups of AE-signals are barely distinguishable, Figure 9b, with the AE-signal generated during loading and unloading are overlapping, as seen more clearly in the insert of the figure. Only 54 out of 9,938 AE-signals recorded during loading and unloading are distinguishable, Figure 9b, all occurred within the two narrow rectangular windows shown at peak load of Figure 9a. All 54 waveforms were 'trains' of AE-signals, as shown in the three representative in the figure. In other words, an alert of imminent fracture could be provided when such a distinguishable group of AE-signals becomes evident.

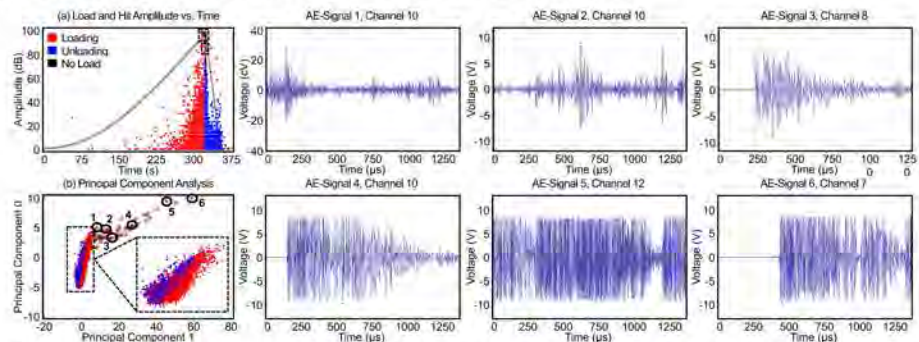


Figure 9. Principle component analyses (PCA0 vs. PCA1), comparing AE-signals recorded during, loading, unloading and by 'noise': a) load-time history with AE-signal amplitude; b) PCA0 vs. PCA1 distinguishing the emission generated during loading, unloading, and by 'noise'; and c) as in (b), for clarity, at a different scale.

## V. CONCLUSION

This study illustrates that acoustic emission conveys a reliable “story” about when and where damage initiates and accumulates and anticipating imminent catastrophic fracture of a large composite panel containing a circular hole which mounted as top skin of a wing box that is subjected to constant moment loading. The presence of existing internal damage, formed during prior extended fatigue loading, was confirmed through early initiation of emission, caused mostly by fretting among the fatigue-generated fracture surfaces. This fretting causes burst-like AE-signal waveforms which are indistinguishable from damage-generated AE-signal waveforms. The propensity of composites to generate ‘trains’ of AE-signals, at rapid rates, is quite high. They occur during both loading and unloading as well as at low- and high-load levels. Since such ‘trains’ of AE-signals are considered by the AE system as a single waveform, the recorded features (e.g., amplitude, duration, frequency spectra, rise time, etc.) of these combined waveforms do not necessarily lend themselves to the conventional correspondence between of waveform features and modes of damage without further post-test analysis of the waveform, e.g., via windowed FFT analyses.

Damage initiated and progressed at two specific sites which were located quite accurately via AE. Imminent fracture could be anticipated based on a combined, four-prong, approach based on information provided by the AE, namely: i) emission accumulation rate; ii) intensity of the AE signals; iii) planar location of the AE sources, and iv) emission distinguished via Principal Component Analysis.

## VI. ACKNOWLEDGMENT

This study was conducted in support of the Cooperative Research and Development Agreement (CRDA) between the Federal Aviation Administration in Atlantic City, New Jersey, and The Boeing Company (Boeing Research & Technology) on bonded repair size limit, with the participation of Drexel University. Drexel was partially supported by a grant from the FAA (grant number 15-G-017). The authors wish to acknowledge the support of John G. Bakuckas, Jr., of the FAA William J. Hughes Technical Center, for facilitating this study and especially note the work of Reewanshu Chadha, of Diakon Solutions, for conducting the mechanical testing program.

## VII. REFERENCES

1. John G. Bakuckas, Jr., Reewanshu Chadha, Paul Swindell, Michael Fleming, John Z. Lin, J.B Ihn, Nihar Desai, Mark Freisthler, Ryan J. Neel, Jonathan Awerbuch and Tein-Min Tan, “*Assessment of Bonded Repairs of Composite Wing Panel Structure*,” 36th Conference & 30th Symposium of the International Committee on Aeronautical Fatigue and Structural Integrity, Krakow, Poland, June 2-7, 2019.
2. Frank A Leone Jr, Didem Ozevin, Jonathan Awerbuch, and Tein-Min Tan, “*Detecting and Locating Damage Initiation and Progression in Full-Scale Sandwich Composite Fuselage Panels Using Acoustic Emission*,” Journal of Composite Materials, June 2013 vol.47, no. 13, pp. 1643 – 1664.
3. Amey Khanolkar, Andrew Bergan, Didem Ozevin, Jonathan Awerbuch, and Tein-Min Tan, “*Acoustic Emission Testing of a Curved Pultruded Rod Stitched Efficient Unitized Structure (PRSEUS) Under Combined Loading*,” Proceedings of the American Society of Composites 27th Annual Technical Conference, Arlington, TX, October 1-3, 2012.

# **Development of damage detection method in type-III hydrogen pressure vessel by acoustic emission**

Takuma Matsuo, Hiroki Orito and Kotaro Hase  
Meiji University, Kawasaki, Japan

## **ABSTRACT**

A type-III pressure vessel constructed using an aluminum alloy liner with a full composite overwrap, is generally used in hydrogen storage tanks at hydrogen refueling stations. However, the evaluation of the fatigue damages in the aluminum alloy layer of the vessel is difficult by the conventional NDT method, because of the effect of the surface CFRP layer. In order to overcome this problem, a damage monitoring method for a type-III hydrogen pressure vessel has been developed by using the AE method. The characteristics of the AE parameters that propagated in the vessel were studied. A small type-III vessel was used as a specimen. Artificial AE signals were produced by laser ablation using a pulse YAG laser. The pulsed laser was irradiated on different cross-sectional layers. As a result, the extraction of the AE signal that was excited in the aluminum alloy layer was successful by using the characteristics of the AE waveform. However, the AE extraction by using weak AE signals was difficult. Further, an optical fiber sensor was employed for wide area monitoring. The optical fiber sensor was wound over the outer surface of the vessel. Artificial AE signals could be detected with a constant and high signal-to-noise ratio when the optical fiber sensor was wrapped over the vessel.

**Keywords:** Type-III hydrogen pressure vessel, fatigue, optical fiber AE sensor, monitoring, waveform classification

## **1. INTRODUCTION**

In recent years, there has been increased attention on using hydrogen as a clean source of energy. In Japan, to promote the proliferation of hydrogen vehicles, the development of hydrogen stations is advancing. Type-III composite pressure vessels are used in hydrogen stations. Figure 1 shows the structure of a type-III composite vessel [1]. The vessel structure comprises of an aluminum alloy liner which is covered with a Carbon Fiber Reinforced plastics (CFRP) helical layer and a CFRP hoop layer. Although the vessel possesses a high strength and an appropriate weight, fatigue cracks are generated during its operation.

In order to prevent accidents caused by fatigue, non-destructive inspections and monitoring of the vessel are important. In standard metal vessels, fatigue cracks are detected and evaluated by ultrasonic testing on the basis of which fatigue life is estimated. However, in a Type-III vessel, it is difficult to evaluate fatigue cracks due to the CFRP layer. Therefore, the acoustic emission (AE) method is considered as a suitable alternative. If the progress of the fatigue cracks can be evaluated by the AE method, it is possible to diagnose the health of the vessel. However, there are few cases where the AE method is applied to a type-III vessel comprising a complicated sectional structure.

In this study, we first evaluate the characteristics of an AE signal propagating through a type-III vessel. We have clarified the propagation velocity and the attenuation of the AE signal in addition to its source locating accuracy and examined the application of the AE method to a

type-III vessel. Further, we have developed a smart accumulator capable of measuring AE signals in a wide range of type-III vessels using an optical fiber AE sensor.

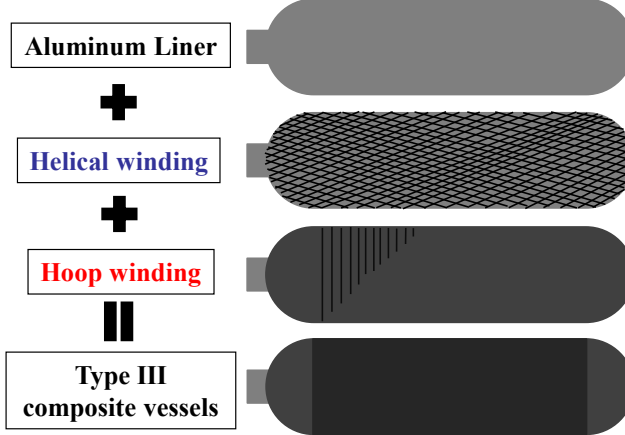


Fig.1 Structure of type-III composite pressure vessel

## 2. CHARACTERISTICS OF AE PROPAGATION IN TYPE-III VESSEL

### 2.1 Source location accuracy

For evaluating the state of the vessel, it is important to detect where the damage has occurred. However, in composite materials such as CFRPs, anisotropy of the velocity of propagation of the material occurs, thus the detection of the source location is difficult. For this reason, in order to perform a detailed source location detection, a source orientation method considering velocity anisotropy is required [2]. However, we considered the extent of the impact of disregarding the anisotropy of the propagation velocity in this test.

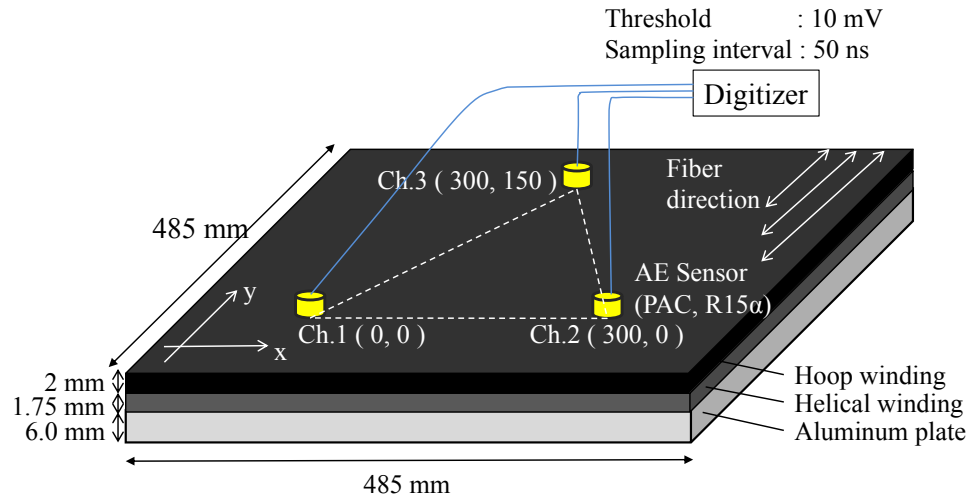


Fig.2 Experimental setup for AE source location in composite plate

Figure 2 shows an experimental setup for the AE source location by the pencil lead breaking method. A flat plate simulating a type-III composite vessel was used, in which an aluminum alloy

plate with a length of 485 mm, a cross ply CFRP plate, and a unidirectional CFRP plate were laminated. The total thickness of the flat plate was 9.75 mm. The orientation direction of the fiber of the unidirectional CFRP plate was considered as the  $y$  axis and the direction perpendicular to the fiber was considered as the  $x$  axis. An R15 a (resonance frequency 150 kHz) AE sensor was used for the experiment. We set three sensors on the plate. In addition, artificial AE signals were excited from the aluminum plate by pencil lead breaking. Fig. 3 shows the AE waveforms detected by each sensor when the AE source was at  $(x, y) = (150, 200)$ . The lines in the figure present the theoretical arrival times of the  $S_0$  mode of the aluminum plate, the  $A_0$  mode of aluminum plate, and the  $A_0$  mode of the CFRP plate, respectively. Meanwhile, the source location was detected using the  $S_0$  mode of the aluminum plate.

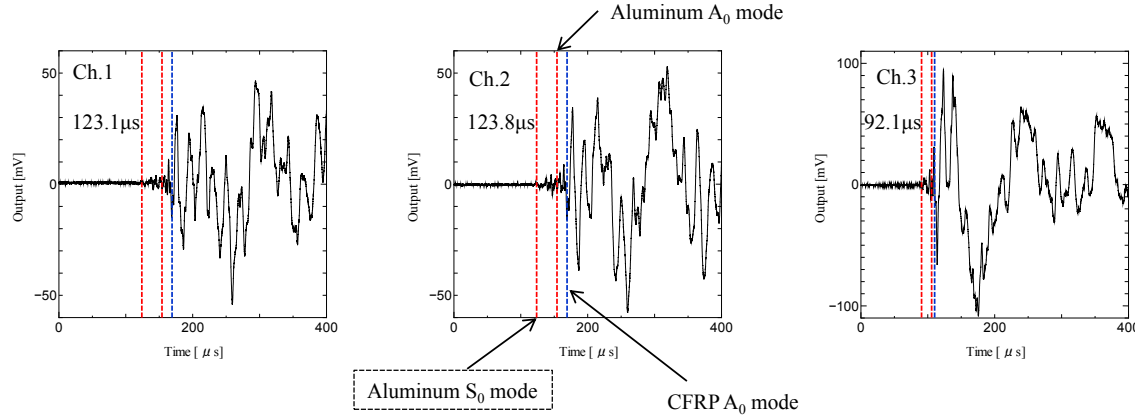


Fig.3 Waveforms detected by three AE sensors produced by pencil lead breaking at  $x = 150$  mm and  $y = 200$  mm

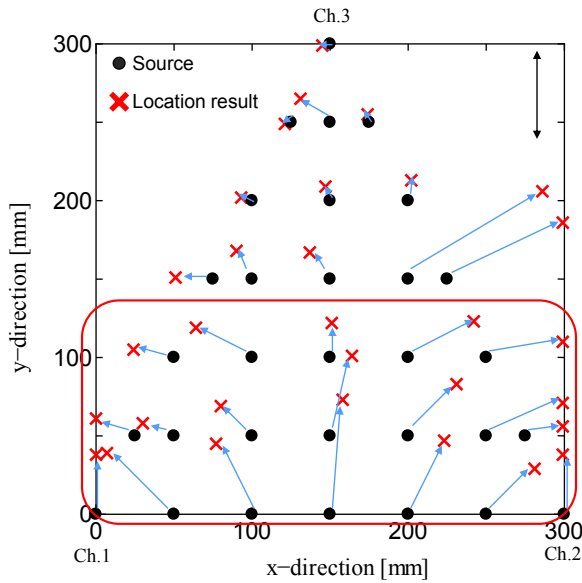


Fig.4 Source location results

Fig. 4 shows the results of the detection of the source location. The average location error calculation of the overall location resulted in an average error of 12 % and a maximum error of 34 %. This error occurred due to the deviation in the arrival time under the influence of the velocity anisotropy due to the presence of the CFRP layer. The first arrival wave packet was

presumed to be caused by background noise. This result indicated that an AE propagation in type-III vessels becomes complicated due to the presence of the CFRP layers, thus it is expected that a highly accurate source location is difficult.

## 2.2 Characteristics of AE waveform originating from different layers

Further, the micro cracks occurring in the vessel were simulated with an artificial AE source and the classification of the AE signal was attempted by using a specimen simulating a small type-III vessel. The experimental setup is exhibited on the left in Fig.5. An opening was provided in the central part of the vessel, and the artificial AE signals were excited by irradiating the cross-section with a pulse YAG laser. The pulsed laser simulated a mode-I type destruction by point focusing at each layer with a power of 1.47 mJ. The pulsed laser was also used for simulation of a delamination by line focusing at the interface between the aluminum liner and the CFRP layer. In addition, as exhibited on the right in Fig. 5, the sensor position was changed from 25 mm to 125 mm, while the fiber orientation direction of the hoop layer was set to 0° and was increased to 90° at 15° intervals.

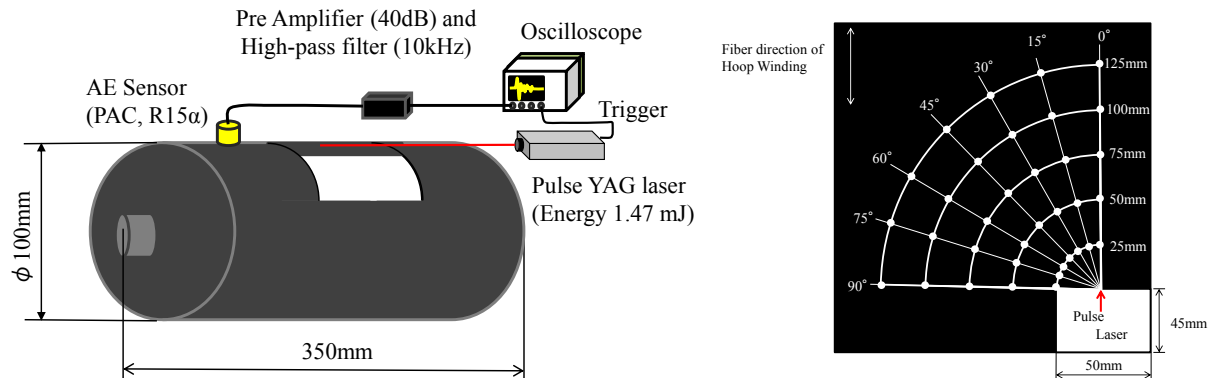


Fig.5 Experimental setup for detecting artificial AE signals propagated in a small type-III vessel

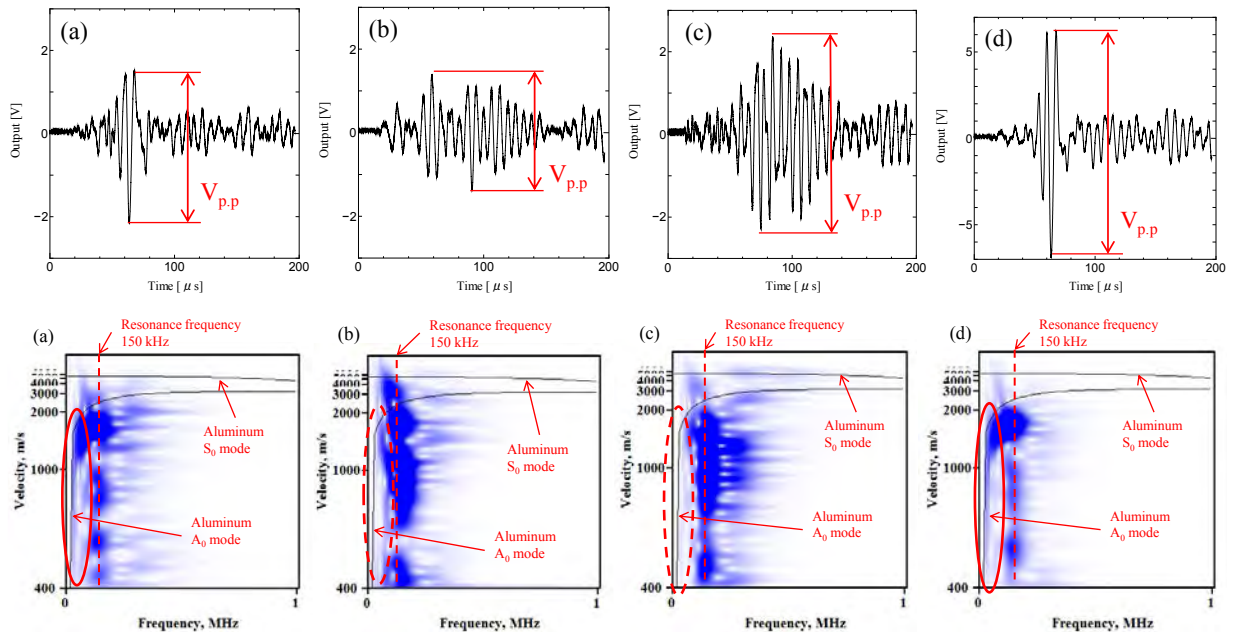


Fig.6 Waveforms and their wavelet contour maps produced at different AE sources

Fig. 6 shows the waveforms and the corresponding wavelet contour maps of each AE source at the propagation angle of  $0^\circ$  and a distance of 100 mm. The AE waveform originating from the aluminum liner had low frequency components. However, it was found that compared to the waveform originating from the aluminum liner, the waveform originating from using the hoop winding as the AE source had higher frequency components. In addition, the waveforms having the characteristics of both an aluminum liner and a CFRP layer as an AE source tended to be detected in a sound source whose interface simulated delamination. They were thus, used as an AE source. Fig. 7 shows the relationship between the peak amplitude of the AE waveform originating from the aluminum liner and from the delamination, with the propagation angle at  $0^\circ$  and  $90^\circ$ . It was found that regardless of the angle and the propagation distance, the peak voltage of the waveform simulating the delamination tended to be larger than the peak voltage of the aluminum liner used as the AE source. By using these features, there is a possibility of extracting the AE caused by the fatigue cracks in an aluminum alloy. However, since the attenuation of the AE signal may vary greatly depending on the angle, there is a possibility that a large number of sensors may be required when monitoring a large vessel.

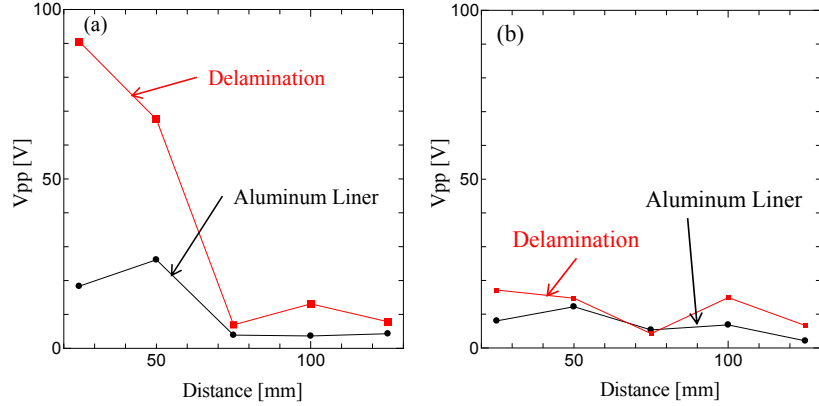


Fig.7 Change in maximum amplitude as a function of sensor distance at angle at  
(a)  $0^\circ$ and (b)  $90^\circ$

### 3. DEVELOPMENT OF SMART VESSEL BY OPTICAL FIBER AE SENSOR

Based on the results obtained so far, in order to quantitatively evaluate the AE signal propagating through the vessel, it is considered that a system capable of measuring a wide range area is necessary. Therefore, we have proposed a system that winds the optical fiber sensor around the outer circumference of the vessel and constructs a smart vessel using the entire vessel as a sensor, thus monitoring the entire vessel. Figure 8 shows the experimental equipment diagram. The optical fiber sensor was wrapped around the hoop winding part located at the outer surface of the small vessel used in the previous section. A pseudo AE signal was excited using a pulse YAG laser with an energy of 3.25 mJ. Each sensor was positioned at 60 mm from the sound source. Figure 9 shows the detected waveform and the frequency spectrum of the PZT sensor and the optical fiber sensor. The difference between the Signal-to-noise (SN) ratio of the optical fiber sensor and the PZT sensor is small, and it is expected that the AE due to the fatigue crack propagation can be detected. Thus, by laying this sensor over a wide area, it is possible to monitor the entire vessel.

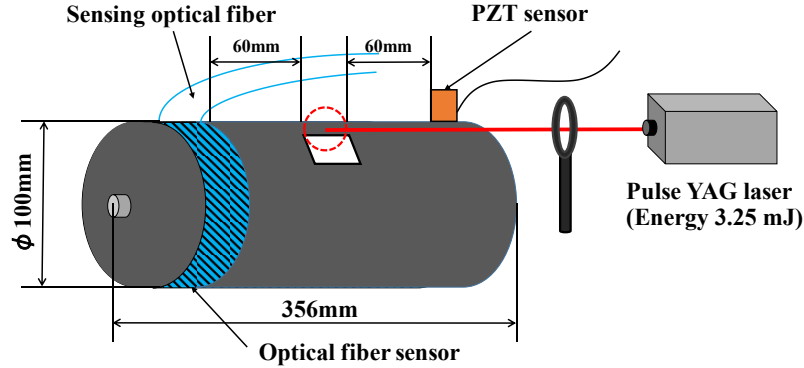


Fig.8 Experimental setup for comparing artificial AE signals detected by PZT sensor and optical fiber sensor

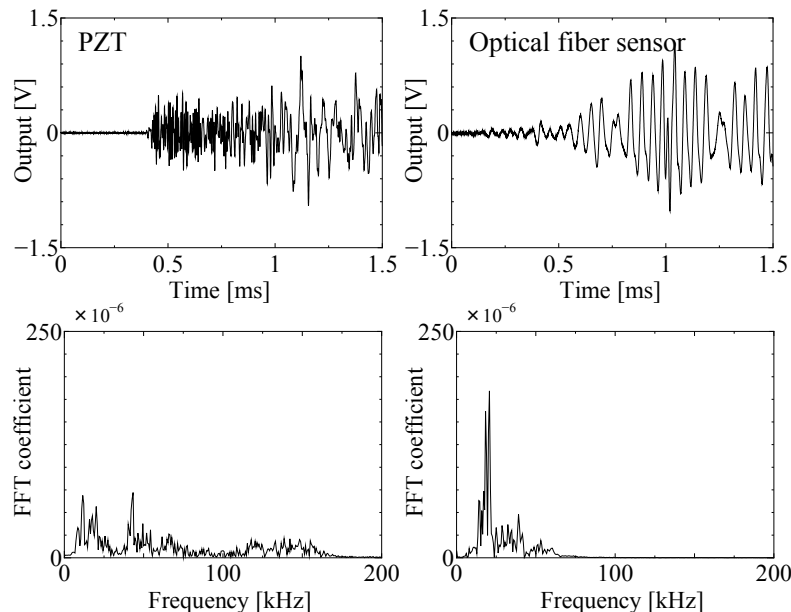


Fig.9 Waveforms and their frequency spectra detected by optical fiber sensor and PZT sensor

#### 4. CONCLUSION

A damage monitoring method for a type-III hydrogen pressure vessel was developed by using the AE method. The detection of the source location disregarding the anisotropy of the propagation velocity was difficult. The extraction of the AE signal that was excited in the aluminum alloy layer was successful by using the characteristics of the AE waveform. An optical fiber sensor was then employed for wide area monitoring. Artificial AE signals could be detected with a constant and high signal-to-noise ratio when the optical fiber sensor was wrapped over the vessel.

#### Reference

- [1] S.W.Kim et., al., Proc. ASME PVP Conf., No. PVP2018-84188, pp. V03BT03A002,(2018)
- [2] Y. Mizutani, et. al., NDT&E International, Vol. 33, (2000), pp. 101-110

# Noise Tolerant and Wireless AE Measurement System for Process Monitoring

Kaita Ito<sup>a</sup>, Kazuki Takahashi<sup>b</sup>, Manabu Enoki<sup>b</sup>

<sup>a</sup>National Institute for Materials Science; <sup>b</sup>The University of Tokyo

## ABSTRACT

Process monitoring is one of the important applications of acoustic emission (AE) method. During manufacturing process of materials and structures, microscopic defects affect their performance and reliability in some cases. AE method is an effective *in-situ* NDE technology for detection of occurrence of such defects. However, there are two problems here. Firstly, AE process monitoring is often disturbed by strong noise. Secondly, cables installation for AE measurement is often forbidden due to operational reason at the site, or it is impossible when the sensors are placed in sealed or rotating parts. The first problem can be suppressed by AE streaming with digital noise filter in the frequency domain. And the second problem can be avoided by wireless measurement. In order to solve both problems simultaneously, a wireless AE measurement system with streaming support was developed in this study. Two channels of streams with about 4 MHz of sampling frequency is available by a battery-powered computer board. Acquired waveforms are immediately transmitted to a high performance remote computer via Wi-Fi to do heavy processing for noise reduction and event detection. The noise level in the acquired waveform was lower than that of the conventional wired system because the wireless computer board was electrically insulated from the external power line. Furthermore, the new wireless system can use the same noise filter with heavy calculation as the conventional wired system. As a result, the new system enabled high effectiveness for process monitoring by high noise tolerance and wireless stream acquisition.

**Keywords:** AE streaming, Process monitoring, Wireless monitoring, Noise tolerance

## 1. INTRODUCTION

Monitoring of materials and structures manufacturing process is an important application of acoustic emission (AE) method because microscopic defects during the process may affect their performance and reliability. However, it is a difficult target for AE monitoring due to heavy vibrations and/or electrical noise from the processing equipment. Under such noisy environment, it is known that AE streaming *i.e.* continuous waveform recording with digital noise filter is an effective solution. Then, the authors have developed an AE measurement system “Continuous Wave Memory” (CWM) that focused on AE streaming with various analysis functions. [1-2]

However, there is another practical problem at the actual industrial sites. Cabling of power and communication lines between the sensors, preamplifiers and the main unit of the AE measurement equipment is often difficult or troublesome at the site. On the contrary, typical wireless AE measurement systems do not support streaming because of limited computing performance and wireless communication bandwidth. Therefore, a novel wireless and battery-driven AE streaming server was developed in this research. In this system, the conventional CWM does not directly connect the sensor but works as a client that receives the AE streams wirelessly transmitted from the server. Therefore, the full set of function of noise filters and waveform analyses of CWM is available in this new system.

## 2. DEVELOPMENT

### 2.1 Realization of wireless AE streaming

AE streaming requires the ability to process large amount of waveform data continuously. The minimum required sampling frequency for AE streaming is 2 MHz because the typical highest frequency component in AE wave is about 1 MHz. One sampling data is normally 2 bytes because the typical resolution of analog-to-digital converter (ADC) is between 10 and 16 bits. Therefore, the minimum required data rate of one channel AE stream is 4 MB/s. Considering the performance of the current battery-driven small computer board, only waveform acquisition and simple processing such as event detection by threshold crossing are available at this data rate. It is impossible to perform a heavy processing like a digital noise filter in frequency domain. On the contrary, wireless transmission of AE streams is available for the latest high speed Wi-Fi (IEEE 802.11ac).

Therefore, the wireless CWM in this study, the battery-driven part works as a simple AE streaming server *i.e.* the acquired waveforms are directly sent wirelessly. All of the waveform analysis is done in the client, which is a high performance computer connected to the power supply. Figure 1 shows the role sharing of the server and client parts of the wireless CWM.

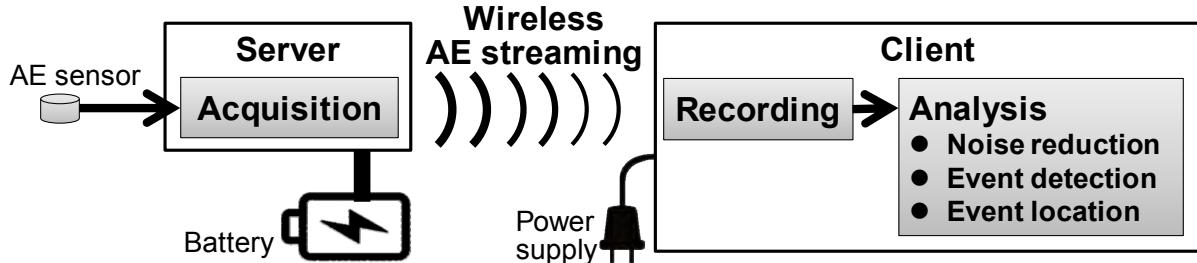


Figure 1: Role of the server and client of the wireless CWM.

### 2.2 AE stream server

An IoT (Internet of Things) board STEMlab 125-14 (Red Pitaya team) was adopted as the mainboard of the server. A simple preamplifier subboard can be attached to the mainboard. Figure 2 shows the data and control flow in the server side. Two sensors can be connected to the server. The range of input voltage is selectable between  $\pm 1$  V and  $\pm 20$  V and the resolution of ADC is 14 bits. Due to the narrow voltage range with high resolution sampling and low noise level of the on-board circuit, accurate waveform acquisition is possible even when the preamplifier is not used. The practical maximum frequency of STEMlab 125-14 for streaming *i.e.* continuous waveform acquisition without any data loss was confirmed as 3.9 MHz by a preliminary experiment. That is, the raw signal of 125 MHz sampling from the ADC was divided by 32 in the FPGA (Field Programmable Gate Array). The acquired continuous waveforms were written in a microSDXC memory card with excellent continuous write performance. The server supports NFS (Network file system) and the client connects to the NFS server and downloads the streams data. It is not described in the official manual, but since the STEMlab 125-14 supports the microSDXC memory, hours of waveforms could be cached in the server.

The footprint of the server was 107 mm  $\times$  60 mm and the weight excluding the battery was about 100 g. Since the power consumption during operation was about 3.8 W, the server could operate for several hours with a small Li-ion battery. Consequently, a wireless AE streaming server with compact size, light weight and sufficient operating time was developed successfully.

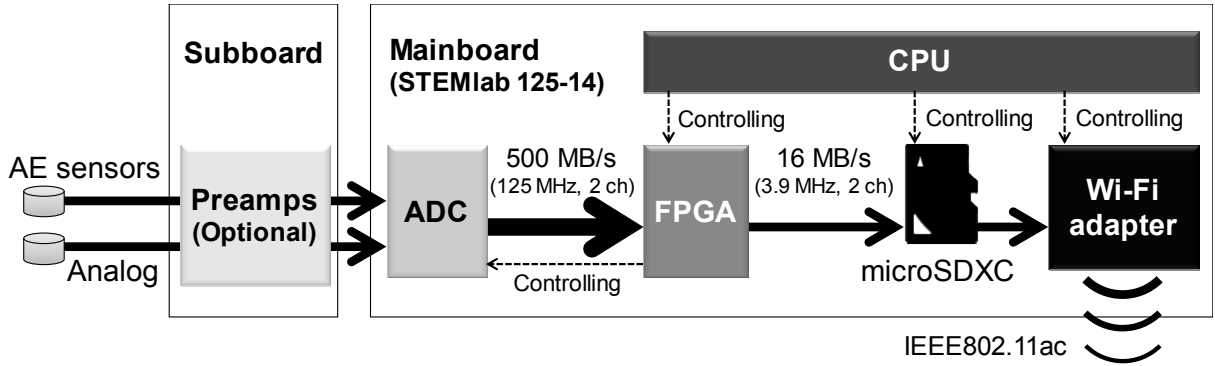


Figure 2: Block diagram of the server part of the wireless CWM.

### 2.3 AE stream client

The conventional wired CWM could be used as the client after a small implementation of server control commands for configuration, starting and stopping of streaming. The full set of analysis functions of the conventional CWM which includes digital noise reduction, event detection and event location is available in the new wireless CWM system.

Various forms of the clients are available. The simplest one is a local client which communicates with the server via Wi-Fi and analyzing the continuous waveforms (see Figure 3(a)). On the contrary, a remote client is also available if there is a broadband router. The remote client can be built on a virtual machine in data center (see Figure 3(b)). In both cases, visualization and downloading of the analysis results is available by a local or remote tablet or laptop computer via Wi-Fi and 4G network since the required traffic is sufficiently small.

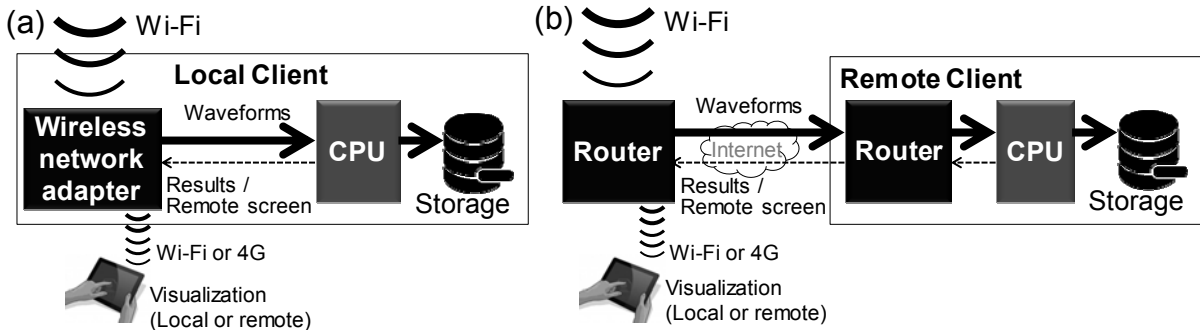


Figure 3: Block diagram of the server part of the wireless CWM.

## 3. VERIFICATION EXPERIMENT

### 3.1 Noise in actual AE measurement

In order to confirm the performance of wireless AE streaming and noise tolerance, wireless CWM was tested in an actual materials manufacturing process. In the verification experiment, two flat plates of magnesium alloy with 2.0 mm thick were joined by friction stir welding (FSW) process. During the process, AE was monitored by the wireless CWM system. The conventional wired CWM was also used for comparison. Heat resistant AE sensors (type AE254SMH177 by Fuji Ceramics) were placed around the welding tool. Channels 1 and 2 were connected to the wireless CWM directly and channels 3 and 4 were connected to the wired CWM via 20 dB

amplifier. A high-pass filter with a cutoff frequency of 100 kHz was applied to the acquired AE streams to eliminate low frequency noise due to vibration.

Waveforms of typical AE events are shown in Figure 4. There was a large difference in noise level between the two. In the wired channels, electrical noise was likely to affect the ADC because the all experimental equipment *i.e.* sensors, preamplifiers and the FSW machine was electrically connected via the power line to the ADC in the wired CWM. The oscillation waveform of the piezoelectric sensors by an electric pulse is difficult to distinguish from the usual burst type AE event due to microfracture in the material. On the other hand, electrical noise was not found in the wireless channels since there was no electrical path through the streaming server.

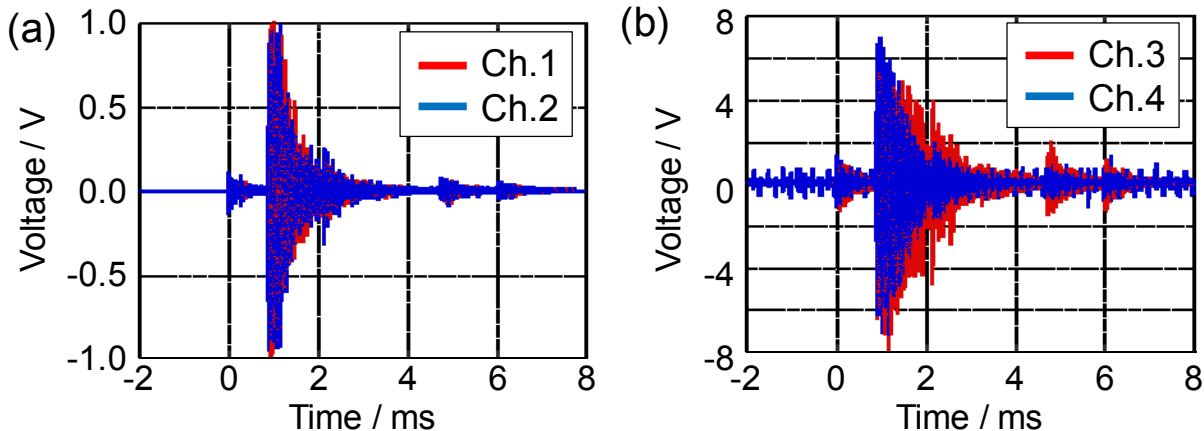


Figure 4: Typical waveform of an AE event recorded by (a) wireless CWM and (b) wired CWM.

#### 4. CONCLUSION

- A novel wireless AE measurement system was developed with streaming support. Two channels of streaming are available with about 4 MHz of sampling frequency by a battery-powered server and high speed Wi-Fi.
- The client as analyzer of the AE stream can use not only a local computer but also a remote virtual computer. Visualization and downloading of the analysis results is available by a local or remote tablet or laptop computer via Wi-Fi or 4G network.
- Electrical noise was not found in the streams by wireless measurement since there was no electrical path through the battery-powered wireless streaming server.

#### ACKNOWLEDGEMENT

This research was supported by JSPS KAKENHI (Grant-in-Aid for scientific research) No. 17K14820. Also, the authors are grateful to Dr. Eitaro Yukutake of Industrial Technology Innovation Center of Ibaraki Prefecture.

#### REFERENCES

- [1] Ito, K., Enoki, M., "Acquisition and Analysis of Continuous Acoustic Emission Waveform for Classification of Damage Sources in Ceramic Fiber Mat", *Materials Transactions*, 48 (2007) 1221-1226.
- [2] Ito, K., Enoki, M., "Analysis of High Active AE Signal by Continuous Waveform Recorder", *Key Engineering Materials*, 353-358 (2007) 2399-2402.

# Sensing and clustering analysis of acoustic emission due to crack rubbing/clapping in fatigue-cracked thin metal sheets

Roshan Joseph, Victor Giurgiutiu

Department of Mechanical Engineering, University of South Carolina, Columbia, USA

## ABSTRACT

Fatigue cracks in metallic structures can cause catastrophic failure to the structure if it is not detected during its early stage. Rubbing and clapping of crack faying surfaces are a potential source for acoustic emission (AE) signals. The vibration of fatigue cracked sheet metal samples were used to induce rubbing and clapping of crack faying surfaces to generate AE signals. The AE signals generated were captured by multiple piezoelectric wafer active sensors (PWAS) bonded to the sheet metal sample in a linear configuration, and source localization was performed to confirm the origin of the AE signals. In some practical cases, the structure would be subjected to external loading while undergoing crack rubbing and AE generation. The sheet metal sample was first axially loaded, then rubbing/clapping was induced through the vibration of the specimen and AE signals were recorded to study the influence of external loading on the AE signals. A large number of AE signals was captured through various cases of AE experiments. To understand the consistency or similarity of the signals, it is necessary to perform a statistical analysis of these AE signals. Pearson correlation was performed for all AE signals in the time domain as well as in the frequency domain to understand the similarity of AE signals. A 2D plot of time domain as well as frequency domain correlation was obtained to depict the similarity in the AE signals.

Keywords: Acoustic emission, AE signal processing, Crack rubbing AE, Correlation of AE signals

## 1 INTRODUCTION

Acoustic emissions (AEs) are the stress waves produced by the sudden internal stress redistribution of the materials caused by the change in internal structure possibly due to crack initiation and growth, dislocation movement, twinning, phase transformation in monolithic materials, fiber breakage, fiber-matrix debonding in composites, etc.[1]. AE signal characteristic is strongly influenced by the source mechanism of the AE. The mechanism of the source is significantly influenced by the composition of the material[2]–[5]. Many researchers studied AE due to various kinds of sources. Wang et al.[6] performed acoustic emission due to rubbing in a rotor-bearing and source localization. Acoustic emission due to progressive damage in a polymer-based composite[7] as well as clustering of AE signals obtained from failure on carbon fiber reinforced plastic (CFRP) specimens was studied[8]. Acoustic emission during various fracture activities was studied to relate the fracture and AE signals [9].

Acoustic emission during fatigue a crack growth event attracted many researchers. The detection of fatigue crack growth can prevent catastrophic failure of structures. Many researchers have studied the AE due to fatigue crack growth[10]–[13]. Zhang et al.[14] studied the acoustic emission signatures of fatigue damages in an idealized bevel gear spline and identified two different AE signal signatures for plastic deformation and crack jump. Bhuiyan et al. [15]–[17] studied the AE signal signatures recorded by PWAS sensors during a fatigue crack growth experiment. Roberts and Talebzadeh [10] discussed the correlation between acoustic emission count rates and crack propagation rates.

The AE signals are generated when a crack growth in metallic structures occurs and several studies have been reported on this, similar to the works presented in the previous paragraph. It

is not obvious that the crack will be always growing and producing the AE signals. If the fatigue loading on the structure is not enough for the crack advancement, the crack may not grow. But, any kind of vibration or fatigue loads which do not cause any crack propagation can produce AE signals when the crack surfaces rub and clap each other. No research works have been reported yet to study the signals generated due to rubbing and clapping of crack faying surfaces of thin metallic plates. This paper discusses AE signal signatures when the faying surfaces of crack rub and clap each other.

The organization of the paper is as follows. Section 2 discusses the experimental setup and methods. The experimental set up for generating the fatigue crack in a 1-mm aluminum plate and the experimental set up for measuring AE signals due to rubbing and clapping of crack faying surfaces are explained in this section. In section 3, the results of Finite Element Method (FEM) analysis of the specimen, as well as the AE signal signatures due to rubbing and clapping of crack faying surface, have been discussed. The paper ends with a summary, conclusions, and future work.

## 2 EXPERIMENTAL SET-UP AND METHODS

### 2.1 Experimental setups

Aluminum 2024-T3 specimen was chosen for manufacturing the test specimen material. The material properties of the specimen were 73 GPa modulus of elasticity, 2767 kg/m<sup>3</sup> density, and 0.33 Poisson's ratio. The aluminum coupons manufactured had dimensions 103 mm width, 305 mm length and 1 mm thickness. 1 mm hole was drilled at the geometric center of the specimen for initiating the fatigue crack. The hole would cause stress concentration at the edges of the hole, and the crack initiation would happen at the hole. Fatigue loading was applied to the specimen to generate the pre-crack. For the pre-crack generation fatigue loading from 22 kN to 2.2 kN at a frequency of 4 Hz was applied. Crack initiation started at approximately 40,600 cycles. The crack grew 20 mm in 400 cycles. After generating the crack in the specimen, four PWAS sensors were bonded on the specimen (Figure 3). One PWAS was bonded very close to the crack at a distance of 6 mm from the crack. This PWAS was bonded at such a close distance so that it can pick up even the weak AE signals originating from the crack. Two other PWAS were bonded at 25 mm distance from the crack in opposite directions, and another PWAS was bonded at 50 mm from the crack. The PWAS bonding configuration, the time of arrival, and amplitude of the signals reaching these PWAS would confirm the AE signal source and geometric spreading of the AE signals.

The experimental setup for generating crack rubbing and clapping in the specimen is presented in Figure 2. For AE generation due to crack rubbing, the fatigue crack grown plate specimen was mounted on a shaker. Continuous sinusoidal excitation was given to the specimen at various frequencies through the shaker. The vibration of the specimen causes the faying surfaces of the crack to rub/clap each other. This rubbing and clapping produce acoustic emission signals.



Figure 1 The specimen with hole mounted on the MTS machine for the generation of crack. Cyclic fatigue loading was applied to generate crack from the hole



Figure 2 The experimental set up for generation of vibration-induced crack rubbing/clapping AE signals. The sinusoidal excitation for vibrating the specimen was generated by function generator. Sufficient power for the vibrating the specimen using vibration

exciter was obtained from the power amplifier. Vibration generated AE signals were captured by using the Mistras AE system.

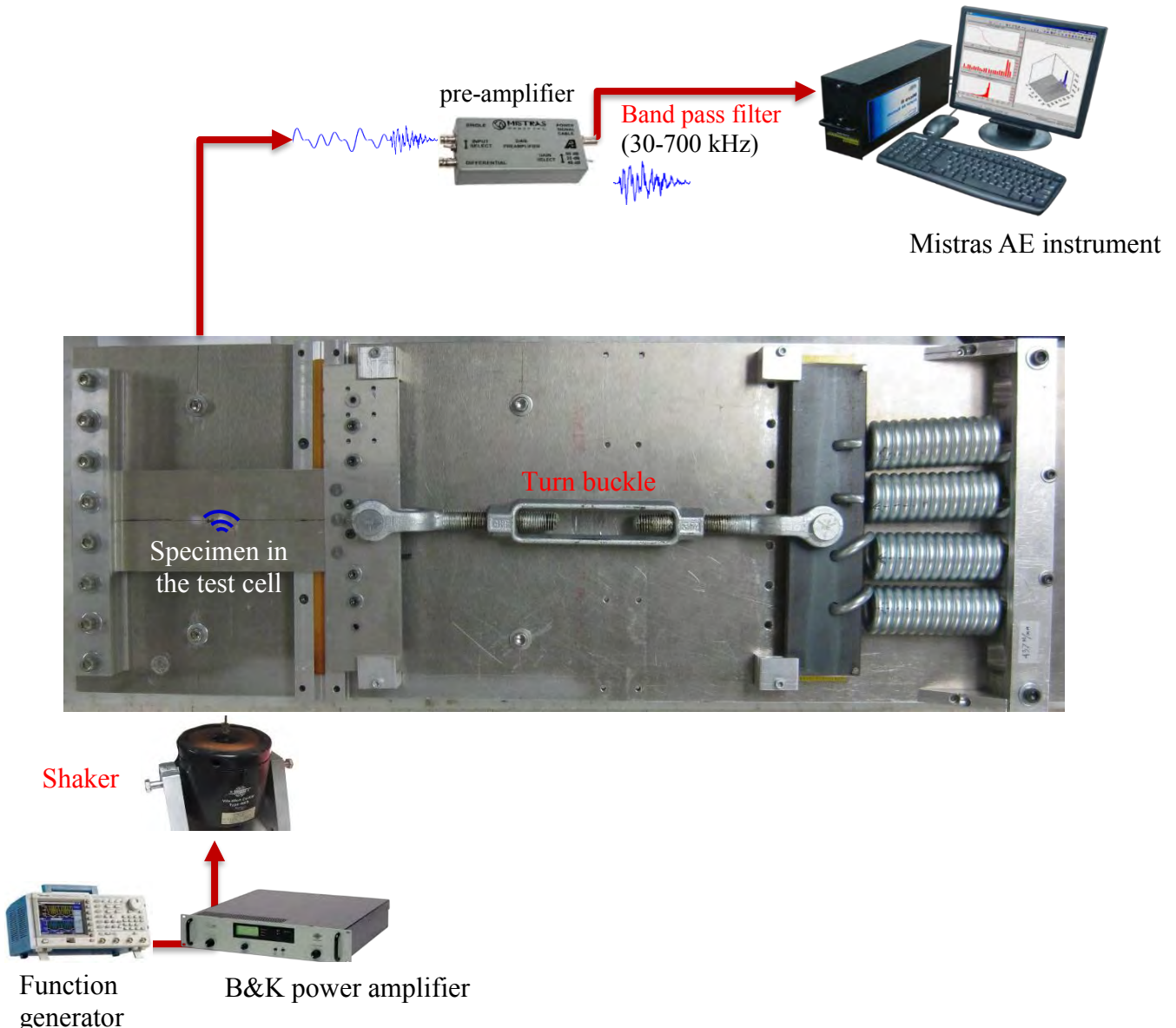


Figure 3 AE measurement test setup in the test cell. Vibration motion is applied to the specimen in the test cell through a shaker. AE signals collected through PWAS bonded to the specimen was passed through pre-amplifier and recorded using Mistras AE system

For the generation of continuous vibration, a function generator was used. For obtaining sufficient voltage of excitation, the signal is amplified using a power amplifier. The amplified sinusoidal signals are fed to a vibration exciter.

The shaker vibrates the plate in the out-of-plane direction causing rubbing/clapping of crack faying surfaces and generation of AE signal due to the rubbing/clapping. The PWAS installed on the

specimen sensed AE hits. Four identical preamplifiers with a built-in bandpass filter (30- 700 kHz) were connected to the sensors. The preamplifier is connected to Mistras AE system. A sampling frequency of 10 MHz was chosen to capture any high-frequency AE signals. AE hits at plate resonance were captured and analyzed. At plate resonances, the possibility of crack rubbing, as well as the threshold of AE signals, are higher, which makes it suitable for AE signal collection and analysis.

In some cases, the cracked specimen may be subjected to external loading. In such cases, the crack would be in an open position. Still, the crack rubbing at the crack tips may induce AE signals. AE signal characteristics in such circumstances need to be studied. A test cell test setup for simultaneously providing axial load and vibrating the specimen was manufactured in house. In Figure 3, a schematic of the setup of the test cell and its important features for mounting AE test specimen and providing axial load is presented. The test cell can arrest two edges of the specimen securely and load the specimen axially through spring loading. The specimen was connected to the spring through a turnbuckle as presented in Figure 3. By using the loading bars, the turnbuckle was turned. Turning the turnbuckle caused extension of the springs and provides the corresponding load to the specimen. The load can be calculated from the spring deflection and the spring constant of the spring. The spring deflection was measured from a knob provided at the spring plate by monitoring its displacement through a measuring scale. After loading the specimen to a specific load, vibration motion was given to the specimen through the shaker attached to it. The AE instrumentation for recording the AE signals is also presented in Figure 3. The AE signals generated by crack rubbing and clapping of the loaded specimen were recorded using a PWAS located 6 mm away from the crack. The signals were fed to the acoustic pre-amplifier with a built-in bandpass filter (30- 700 kHz) and then fed to Mistras AE instrument. Recorded AE signals were post-processed and analyzed.

## 2.2 Pearson correlation coefficient (PCC) of two signals

A large number of AE signals are generated due to rubbing and clapping of crack faying surfaces. Pearson correlation analysis was performed to compare the large number of AE signals. The correlation coefficients of two-time series/frequency series data are calculated using the following PCC expression.

$$\rho(A, B) = \frac{1}{N-1} \sum_{i=1}^N \left( \frac{A_i - \mu_A}{\sigma_A} \right) \left( \frac{B_i - \mu_B}{\sigma_B} \right) \quad (1)$$

Where,  $A$ =time domain signal  $A$ ,  $B$ =time domain signal  $B$ ,  $\mu_A$ = mean of signal  $A$ ,  $\mu_B$ = mean of signal  $B$ ,  $\sigma_A$ = standard deviation of signal  $A$ , and  $\sigma_B$ = standard deviation of signal  $B$ . Two separate correlation coefficients were calculated, using time domain as well as frequency domain data. 2D scatter plots of time domain PCC vs. frequency domain PCC were constructed.

## 3 RESULTS AND DISCUSSION

For generating strong AE signals during rubbing and clapping of crack surfaces, there must be active interaction between the crack faying surfaces. The resonant frequencies of specimen vibration are appropriate for the generation of strong displacements in the specimens, which can cause active interaction between the crack faying surfaces. FEM modal analysis of the cracked specimen was performed to find out the resonant frequencies of the specimen. The specimen modeled and boundary conditions imposed to the specimen for performing FEM modal analysis are presented in Figure 4. The fixed boundary condition is applied at the support hole of the

specimen which was used to connect the shaker attachment to the specimen by arresting all degrees of freedom. From FEM analysis, the first five resonance frequencies of the specimen were recognized as 28.2, 37.8, 93.1, 112.3 and 188.4 Hz respectively. It was presumed and observed that this resonant frequencies and corresponding strong displacement causes strong crack faying surface motions which generated strong AE signal. We observed strong AE signal generation at 35 Hz and 180 Hz frequency of vibration of the specimen.

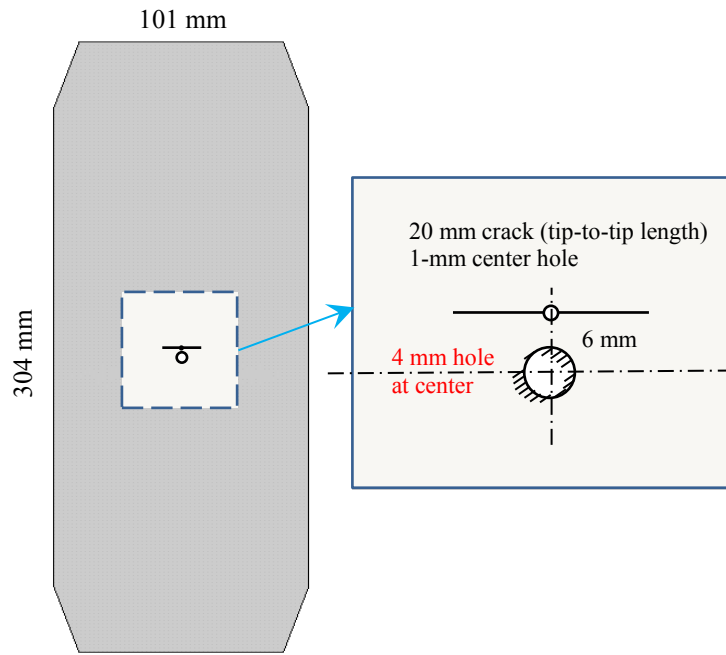


Figure 4 The specimen and boundary conditions given for performing modal analysis of specimen attached to shaker. Fixed boundary conditions are given at the support hole corresponding to the vibration shaker support.

Vibration excitation was given to the specimen at 35 Hz by using a shaker, and the vibration induced the crack faying surface rubbing and clapping. The induced rubbing and clapping of the crack faying surfaces cause the excitation and propagation of AE signals in the specimen. The signals were sensed using PWAS sensors bonded 6-mm from the crack. The PWAS sensed AE signals were recorded using the Mistras AE system. A large number of AE signals were recorded during a short period of time. The signals collected were used to perform a correlation analysis by choosing a particular signal as the basis signal. The correlation analysis shows that the signals are similar. The correlation of AE signals and one typical AE signal collected is presented in Figure 5a and Figure 5b. The AE signal signature is observed to be wideband. Peaks in the frequency spectrum were observed at 100 kHz. At frequency spectrum between 300- 400 kHz, a peak in the frequency spectrum by gradual increment and decrement was also observed. The differences in signals are due to the uncertainty in AE source characteristic at the crack faying surfaces corresponding to various events. The minor difference in AE signal infers that, even though there is uncertainty in AE source characteristic which generates the AE signals, the source characteristics are within a tolerance limit.

To study the effect of the frequency of vibration of the specimen on the AE signal, another frequency of vibration of the specimen was also considered. AE signals received by PWAS when the plate is vibrated at 180 Hz frequency is presented in Figure 5c and Figure 5d. We observe that the frequency spectrum of the AE signals is wideband frequency spectra. At 180 Hz vibration of the specimen, a peak frequency of the AE signal spectra approximately at 100 kHz was observed similar to AE signal recorded at 35 Hz vibration. A gradual increase and decrease of frequency spectrum between 300- 400 kHz were also observed. AE signals were observed to have a similar signature.

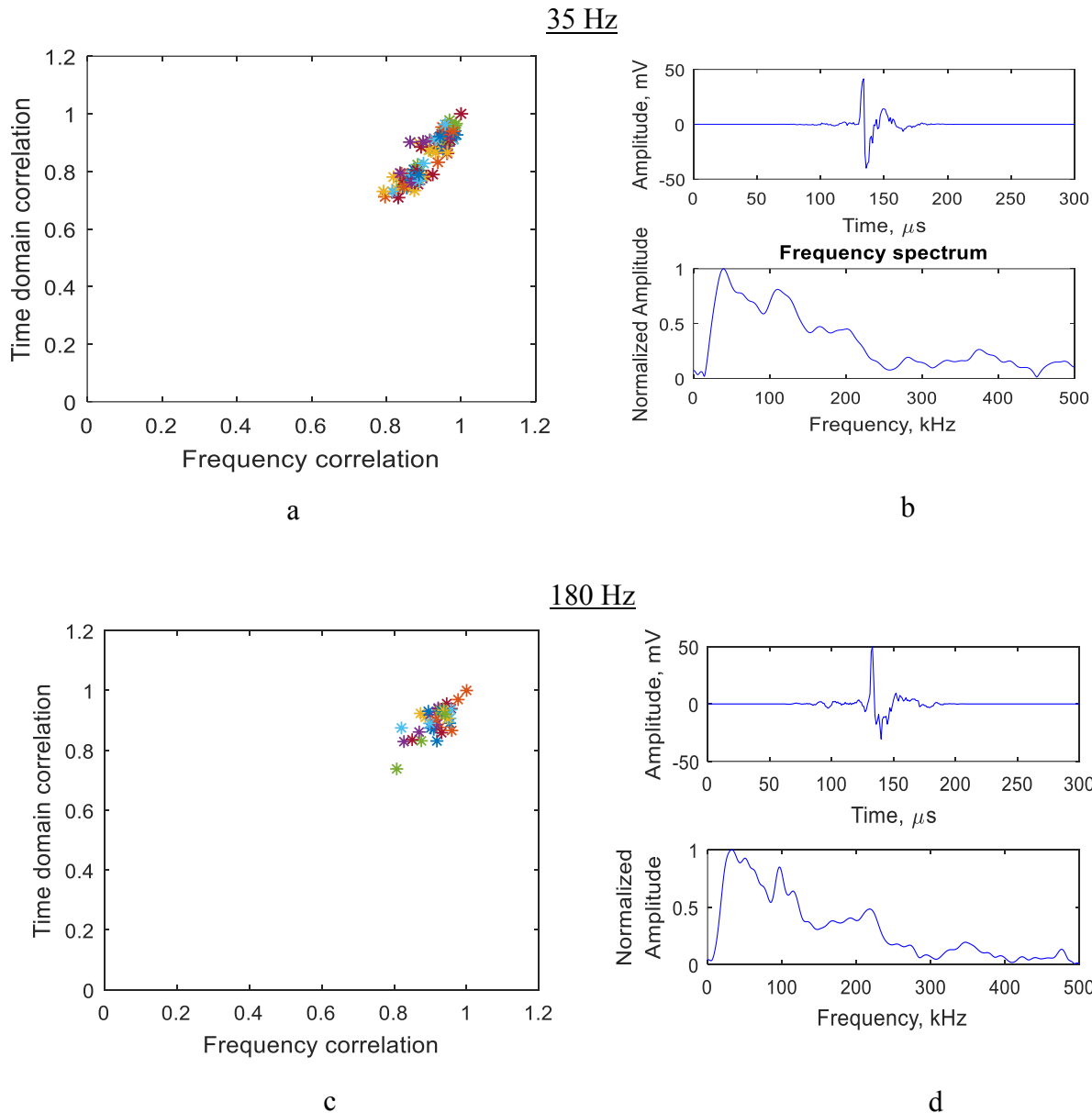


Figure 5 AE signals generated due to vibration of specimen at various frequencies a) Correlation of AE signals generated due to the 35 Hz specimen vibration induced crack rubbing/clapping b) Sample AE signal at 35 Hz vibration c) Correlation of AE signals

generated due to the 180 Hz specimen vibration induced crack rubbing/clapping d)  
Sample AE signal at 180 Hz vibration

The crack faying surfaces formed during the fatigue experiment are very rough in texture with sharp peaks and valleys. The vibration of the specimen causes the sharp peaks and valleys of the crack faying surfaces to hit each other and generate AE signals. Hence the AE signal generation source can be considered as a point force excitation source or a point source. AE signals are generated by rubbing of crack faying surfaces at a point. Even at different frequencies the source characteristic or the mechanism of ultrasonic AE signal generation may remain the same since it is a point source excitation. Hence theoretically, it is not very likely that the AE signal signature may differ at different vibration exciter frequencies. A comparison of the AE signal signature at 35 Hz vibration and 180 Hz vibration can be observed from Figure 5b and Figure 5d. Clear similarities in AE signals and signal frequency spectrums are observed in the figure. The AE signal rise time, as well as the duration of the signal, are observed as approximately the same. Frequency spectrums of both signals were found to be very similar to broadband nature and to have very similar peaks and valleys.

To study the effect of external load on the rubbing/clapping AE signal signature the specimen was mounted on the test cell, axially loaded and vibration excitation was applied. An axial load of 5kN is applied to the specimen by loading the specimen by turning the turnbuckle and applying the spring load. Four springs are arranged parallel to each other as presented in Figure 12. The effective spring constant of the springs is 437 N/mm. The spring loading is provided by turning the turnbuckle between the specimen and the spring. The turnbuckle was turned so that the spring deforms 11.5 mm, providing 5 kN load to the specimen. The extension of the spring monitors the effective load through a needle attached near the spring on the spring plate. After loading the specimen, the specimen was vibrated by the vibration exciter. A higher voltage of excitation was required to produce AE signals compared to specimen mounted in the test cell without any load. The AE signals were collected and the correlation of the AE signals is presented in Figure 14. The signals were found comparable to the AE signals obtained with the no-load case as well as the AE signal generated due to the unconstrained specimen vibration case. The signal is observed as wideband in frequency spectra with a higher amplitude at low-frequency range. Signals had a peak in the frequency spectrum at approximately 100 kHz. A peak in the frequency spectrum is observed between 300 kHz and 400 kHz. But the frequency response between 100 to 200 kHz has been reduced. The major frequency content is observed below 100 kHz, similar to the case of unloaded specimen rubbing and clapping AE signals. The signal correlation is found to be stronger compared to the case of no-load. The reason for such a strong correlation is hypothesized as follows. When the specimen is in a loaded condition, the crack will be in an open position. The vibration exciter causes relative motion of crack faying surfaces, but the rubbing between the two surfaces takes place only at the crack tips since all the other location of the crack is in open position. Hence the point source excitation will be happening only at the crack tips, and the excitation will be more consistent compared to the excitation when the crack is in the closed position.

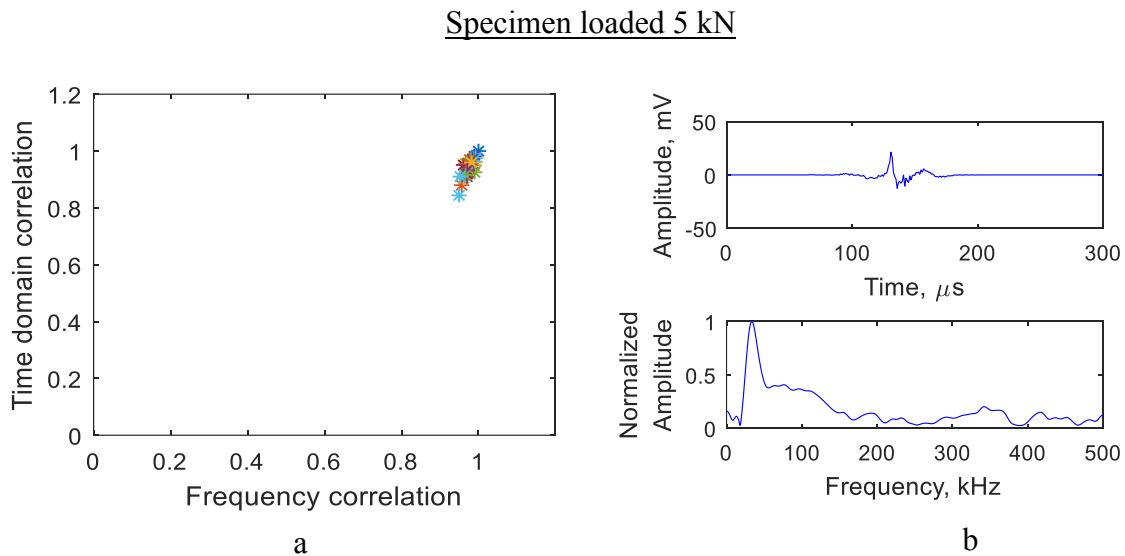


Figure 6 AE signal generated due to the vibration of the specimen under axial tension a) Correlation of AE signals generated due to the vibration induced crack rubbing/clapping b) Sample AE signal at 35 Hz vibration

#### 4 SUMMARY CONCLUSIONS AND FUTURE WORK

##### 4.1 Summary

A Fatigue crack in Al 2024-T3 specimen was generated by cyclic fatigue loading. Fatigue loading of 22 kN with an R ratio of 0.1 was applied for the generation of a fatigue crack. The fatigue loading was continued until the tip to tip crack length is 20 mm. FEM harmonic analysis was performed to analyze the resonant frequencies of the cracked specimen. A PWAS sensor was installed on the specimen at a distance of 5-mm from the crack. The specimen was attached to a shaker table, and vibration excitation was applied at the resonant frequencies of the specimen to generate AE signals due to crack rubbing/clapping. The AE signals generated were recorded using the PWAS and Mistras AE system. Correlation analysis was performed on the signals to identify the change in AE signals and variation in the asperity of the AE signal source. AE signals at 35 Hz and 180 Hz specimen vibrations were studied. AE signals in the specimen under load are also studied

##### 4.2 Conclusions

Resonant frequencies of the specimen are suitable for active rubbing and clapping of the crack faying surfaces. Specimen resonant frequencies do not affect the AE signal signature strongly. Correlation analysis can conveniently quantify the difference in a large number of AE signals. The difference in AE signal signature would correspond to the difference in the AE source characteristics. Close clustering of AE signals is obtained when the vibration AE was generated in an axially loaded specimen. When the crack is in a closed position the rubbing/clapping happens throughout the crack length. This will cause more change in the asperity of the AE signal source as well as AE signal generated from the source. When the crack is in open position, only the crack tips participate in the rubbing/clapping. This will cause less change in asperity of the AE

signal source as well as AE signals generated from the sources, resulting in a close correlation of AE signals.

## 5 REFERENCES

- [1] M. Huang., L. Jiang., P. . Liaw., C. . Brooks., R. Seeley., and L. . Klarstrom., "Using Acoustic Emission in Fatigue and Fracture Materials Research," *Mater. Res.*, vol. 50, pp. 1–13, 1998.
- [2] T. Ohira and Y.-H. Pao, "Quantitative Characterization of Microcracking in A533B Steel by Acoustic Emission," *Metall. Trans. A*, vol. 20, no. June, pp. 1105–1114, 1989.
- [3] D. Healy, R. R. Jones, and R. E. Holdsworth, "Three-dimensional brittle shear fracturing by tensile crack interaction," *Nature*, vol. 439, no. January, pp. 3–6, 2006.
- [4] C. Kao, F. C. S. Carvalho, and J. F. Labuz, "Micromechanisms of fracture from acoustic emission," *Int. J. Rock Mech. Min. Sci.*, vol. 48, no. 4, pp. 666–673, 2011.
- [5] R. Joseph, M. Y. Bhuiyan, and V. Giurgiutiu, "Acoustic emission source modeling in a plate using buried moment tensors," *Proc. SPIE (Health Monit. Struct. Biol. Syst.)*, vol. 10170, no. May, pp. 1017028-1–8, 2017.
- [6] Q. Wang and F. Chu, "Experimental determination of the rubbing location by means of acoustic emission and wavelet transform," *J. Sound Vib.*, vol. 248, no. 1, pp. 91–103, Nov. 2001.
- [7] M. Bentahar and R. El Guerjouma, "Monitoring progressive damage in polymer-based composite using nonlinear dynamics and acoustic emission," *J. Acoust. Soc. Am.*, vol. 125, no. 1, p. EL39-EL44, 2009.
- [8] M. G. R. Sause, A. Gribov, A. R. Unwin, and S. Horn, "Pattern recognition approach to identify natural clusters of acoustic emission signals," *Pattern Recognit. Lett.*, vol. 33, no. 1, pp. 17–23, Jan. 2012.
- [9] S. M. Cousland and C. M. Scala, "Acoustic emission during the plastic deformation of aluminium alloys 2024 and 2124," *Mater. Sci. Eng.*, vol. 57, no. 1, pp. 23–29, Jan. 1983.
- [10] T. M. Roberts and M. Talebzadeh, "Acoustic emission monitoring of fatigue crack propagation," *J. Constr. Steel Res.*, vol. 59, no. 6, pp. 695–712, Jun. 2003.
- [11] T. M. Morton, R. M. Harrington, J. G. Bjeletich, L. Palo, and P. Alto, "Acoustic emissions of fatigue crack growth," vol. 5, pp. 691–697, 1973.
- [12] S. Deschanel, W. Ben Rhouma, and J. Weiss, "Acoustic emission multiplets as early warnings of fatigue failure in metallic materials," *Sci. Rep.*, no. September, pp. 1–10, 2017.
- [13] T. M. Roberts and M. Talebzadeh, "Fatigue life prediction based on crack propagation and acoustic emission count rates," *J. Constr. Steel Res.*, vol. 59, no. 6, pp. 679–694, Jun. 2003.
- [14] L. Zhang, D. Ozevin, W. Hardman, and A. Timmons, "Acoustic Emission Signatures of Fatigue Damage in Idealized Bevel Gear Spline for Localized Sensing," *Metals (Basel)*., 2017.
- [15] M. Y. Bhuiyan and V. Giurgiutiu, "The signatures of acoustic emission waveforms from fatigue crack advancing in thin metallic plates," *Smart Mater. Struct.*, vol. 27, no. 1, p. 15019, 2018.
- [16] Y. Bhuiyan, J. Bao, and B. Poddar, "Toward identifying crack-length-related resonances in acoustic emission waveforms for structural health monitoring applications," 2018.
- [17] M. Y. Bhuiyan and V. Giurgiutiu, "Experimental and Computational Analysis of Acoustic Emission Waveforms for SHM applications," in *11th International Workshop on Structural Health Monitoring*, 2017, pp. 1–7.

# Progress in Sensitivity Verification of AE Sensors

Kanji Ono

Department of Materials Science and Engineering, University of California, Los Angeles  
(UCLA), Los Angeles, CA 90095 United States

## ABSTRACT

Recent progress in AE sensor characterization studies is summarized. These efforts point to practical approaches for the calibration of receiving sensitivities by directly contacting (face-to-face) a reference transmitter and a sensor under test (SUT). This method is for normally incident waves and the displacement or velocity of the reference transmitter is measured by a laser technique, similarly to that prescribed by ISO16063-11 for accelerometer calibration. As the reference transmitter, a heavily damped ultrasonic transducer, available from multiple sources, is used. The transmission sensitivities by a laser interferometer and a laser vibrometer showed a good agreement, so either can be used. By coupling an SUT in a controlled manner, its receiving sensitivity is determined. Over thirty models of AE sensors have been characterized using the present method and their receiving sensitivities found to be consistent with those from the Hill-Adams method, a variation of reciprocity techniques. When one obtains a reference transducer with its transmission sensitivity characterized, the remaining parts of calibration procedures can be conducted even outside of metrology laboratory. That is, a practical sensitivity verification is possible with a traceability to laser-based measurements of displacement or velocity. A variation of the face-to-face method is to insert a buffer medium between a reference transmitter and an SUT. This is inappropriate because of diffraction loss, which is dependent on SUT size, frequency and buffer thickness. A parallel method is available for the detection of plate (Lamb) waves and bar waves, again starting from laser-based measurements. It is suggested that a cooperative effort is undertaken involving multiple organizations to establish national/international standards for sensitivity verification of AE sensors.

**Keywords:** AE sensors, laser interferometer, vibrometer, wave modes, sensitivity verification.

## 1. INTRODUCTION

Efforts to standardize calibration methods for AE sensors have a long history, going back to the seismic pulse method of Breckenridge et al. (1). This seminal work led to two ASTM standards (2,3) for surface wave sensing (also being listed in ISO). These and other early works can be found in (4). At sensor manufacturers, practical sensor characterization has been conducted by direct contact (face-to-face) methods using a reference transducer that was calibrated by hydrophone replacement procedures (5,6). This approach is for normally incident longitudinal waves only and has recently been updated by the use of laser metrology methods (6-9). Laser interferometer or vibrometer can measure surface displacement or velocity without water immersion needed in the hydrophone calibration. It can also obtain spatial variation of the displacement or velocity over the reference transducer. The laser-based calibration methods were extended to guided wave sensing (10,11). Another approach used is a variation of classical reciprocity calibration methods developed for reciprocal transducers. This method, proposed by Hatano and coworkers (12,13), used three transducers and assumed all three to be reciprocal. This reciprocity condition was shown to be absent for typical AE sensors, invalidating the Hatano method (14). Hill and Adams (15) relaxed this condition for a sensor under test (SUT), but required the ratio of transmission and receiving sensitivities of one of the three to be known, mandating

laser-based measurements. This Hill-Adams version of the reciprocity calibration method produced results in agreement with those of the laser-based direct contact methods (6,7).

Presently, three methods can provide AE sensor calibration. However, no national standards agency offers the calibration service for the seismic pulse method, making it desirable for the two other methods to be standardized. Of the two, the direct contact method is preferred since it is applicable to guided wave cases and needs fewer sensor coupling per calibration. Below, the basic calibration procedures are summarized, representative results are shown and finally items needed to be included in a standardization document are listed.

## 2. CONTACT CALIBRATION METHODS

For the calibration with normally incident longitudinal waves, a well damped broadband ultrasonic transducer needs to be excited either by short pulses, continuous sinewaves of varying frequency (Chirp) or short-duration, stepped frequency sinewave trains. The surface displacement or velocity of the transducer is measured using a laser interferometer or laser vibrometer. The input voltage signals and laser device output are used to define transmission sensitivity. Next, an AE SUT is coupled to the transmitter surface. The output from the SUT is obtained with the transmitter excited in the same way as in the first step. The SUT receiving sensitivity can be determined using the SUT output and the transmitter output since the input voltage spectra cancel out. The computation procedures of both transmission and receiving sensitivities involve the frequency domain spectra, utilizing fast Fourier transform (FFT). This procedure was described in (6,7).

For guided wave calibration, a suitable transfer medium is needed. Surface wave calibration requires a large transfer medium and is excluded here. One needs a long bar with flat surface(s) or a large plate with a thickness similar to intended structures, to which an SUT is to be mounted. On one end of the bar or plate, a broadband ultrasonic transducer needs to be coupled and excited as in the normal incidence case. Select a position suitable for SUT installation, measure displacement or velocity of the bar or plate either by using a laser device or a calibrated point-contact AE sensor. Next, install an SUT at the designated position and measure its output with the transmitter excited in the same manner as in the initial step. The SUT receiving sensitivity can be obtained by spectral division as above. This procedure was described in (10,11).

## 3. RESULTS

More than 50 sensors for AE application have been characterized using the two methods given in Sec. 2 and results for 27 have been reported (6,7,10,11,14). For some, low frequency responses were also reported and the origins of observed frequency dependence of receiving sensitivities were discussed (7). Receiving sensitivities of four representative sensors are given below. Each sensor's responses for normally incident longitudinal waves are shown in part a) and for guided waves in part b). The latter is an average of eight spectra corresponding to Lamb and bar waves, symmetric and asymmetric modes and two thicknesses. All of the results below were obtained using pulse excitation of a broadband transmitter. Limited comparison between results of pulse and sinewave excitation (7) indicated good agreement between receiving sensitivities from the two excitation methods.

Two wideband sensors in Fig. 1 represent a well damped smooth response (V103) and a multiple resonance type (WD) that gives a series of high sensitivity peaks. Guided wave responses are completely different. Two resonant sensors show a series of high sensitivity peaks for normal incidence case, but enhanced low frequency response to guided waves.

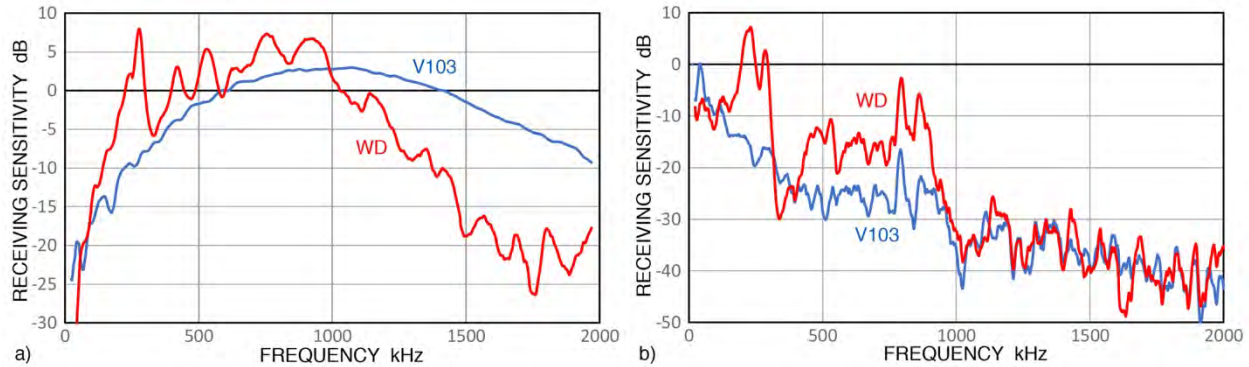


Fig. 1 Receiving sensitivity in dB in reference to 0 dB at 1 V/nm for Olympus V103 (blue) and Physical Acoustics WD (red). a) Normal incidence (data from ref. 6). b) Guided waves (data from ref. 11).

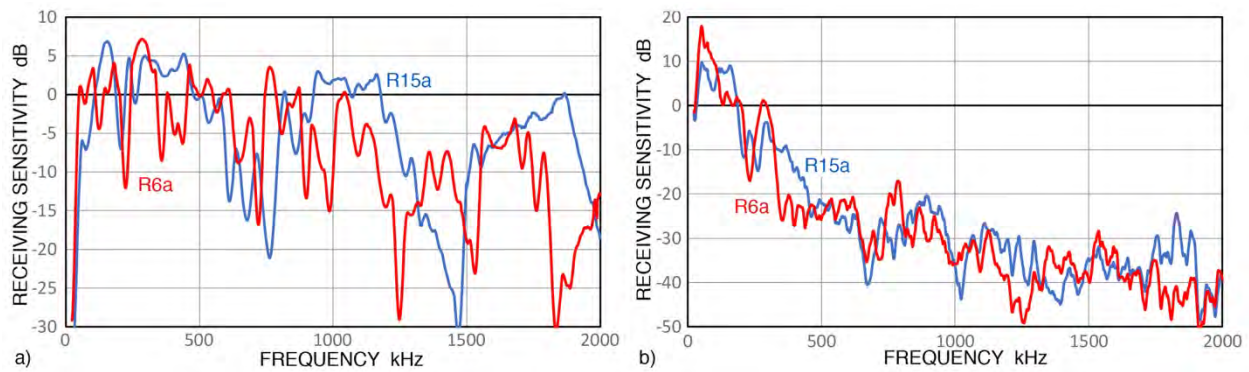


Fig. 2 Receiving sensitivity for Physical Acoustics R15a (blue) and Physical Acoustics R6a (red). a) Normal incidence (data from ref. 6). b) Guided waves (data from ref. 11).

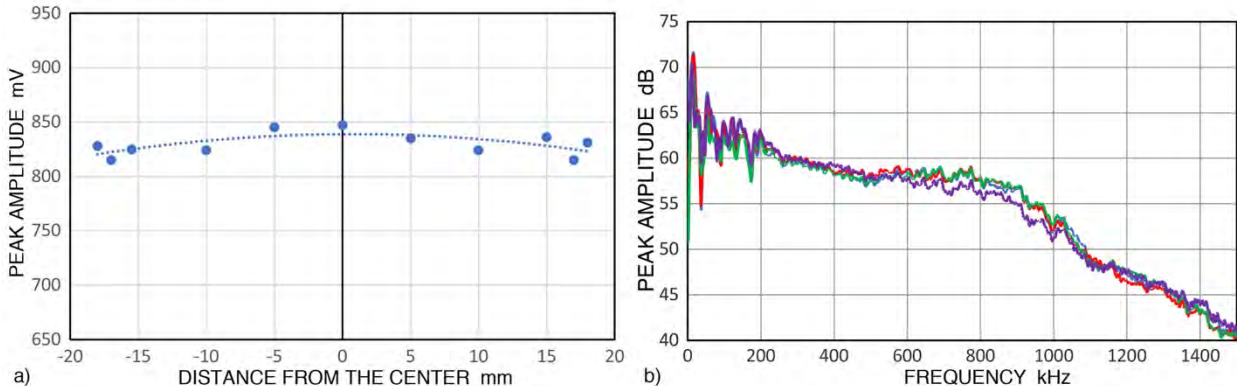


Fig. 3 a) Peak amplitude of KRN sensor output vs. position on the surface of Olympus V192 transmitter under pulse excitation. Dotted curve is a parabolic fit, slightly rising at the center. Maximum and minimum peaks differed by 0.36 dB. b) Frequency spectra of received signals (0 dB at 1 mV). At center (blue curve), at 5 mm (red), at 10 mm (green) at 18 mm (purple).

#### 4. PREPARATION FOR STANDARDIZATION

##### 4.1 Transmitter and its characterization

1. Use a broadband ultrasonic transducer having no major sensitivity dips within the intended calibration frequency range. When one needs to cover up to 2 MHz, select a transducer with its

nominal center frequency of 1 MHz or higher. Our experience suggests Olympus V192 transducer (1 MHz, 38-mm diameter) to be optimal with its smooth output spectrum and anti-resonance dip above 2 MHz, although several others, notably Olympus V104, function similarly well (14).

2. The transmitting transducer must have its size larger than the size of SUT. Experience suggests 38-mm diameter (V192) gives most uniform displacement output, while 25-mm diameter (V104) is satisfactory since most AE sensors have sensing areas of 13-mm diameter or less.
3. The use of laser metrology devices for accelerometer calibration is described in an international standard document, ISO16063-11 (16). This can serve as a useful template for laser uses for AE sensor calibration.
4. In the guided wave calibration, a transmitter is attached to a buffer medium of a bar or plate. This can be with glue or by a mechanical holder, but re-calibration is needed after each attachment.
5. The number and location of laser measurements need to be specified. In our interferometry works using Thales SH-140 (6,7), positions have to be aligned manually and measurements were mostly limited to the center point. The output uniformity was evaluated using a point-contact sensor (KRN BBPCP). Up to 1 mm from the edge of active area of V192 transducer, the responses differed less than  $\pm 0.18$  dB, as shown in Fig. 3a. The spectral output was within  $\pm 1$  dB band (Fig. 3b). Thus, the center responses have been used in all our tests. Vallen reported on the uniformity of the surface velocity output using a laser vibrometer (8,9). Many measurement points allowed him to define the surface responses accurately, averaging on coaxial rings. For a 25-mm transducer, 145 points were used. For well-behaved transducers, the center point only testing appears adequate, but further study should be made as to the optimal number of measurements needed.
6. In using a pulse excitation method, a step voltage pulse should be avoided since it introduces an artefact in FFT. An addition of a damping resistor of 5 to 50 ohms in parallel to the transducer can keep the pulse short (less than several  $\mu$ s).
7. The level of excitation voltage applied on a transmitting transducer depends on the sensitivity of laser devices and on the safe limit from the transducer manufacturer. Peak voltages of pulses used have been under 400 V, producing up to 10 to 15 nm displacement with Olympus transducers. For a 500-kHz transducer, it was possible to apply up to 1.5 kV sinewave pulse without damaging it. However, it is prudent to limit to less than 200 V for those with nominal frequency above 2 MHz. Some guidelines will be helpful.
8. Proper digitization is needed to record transducer input and output voltages. With advances in digital oscilloscope, offering automatic interpolation, even 8-bit resolution may be adequate. Whether 12-bit or 14-bit resolution is required needs to be considered. Rate of digitization controls the resolution of frequency domain signals. We used 2 or 8 ns interval with satisfactory outcome even for low frequency testing in order to keep the frequency interval identical. A minimum sampling rate may need to be specified.
9. Temperature of transducer during laser measurements needs to be recorded and reported since piezoelectric devices are sensitive to temperature. This also applies to SUT.
10. For guided wave calibration, a rectangular aluminum bar of 1:4 ratio (e.g., 6.4 mm x 25.4 mm or 12.7 mm x 50.4 mm and 1 to 3 m length) worked satisfactorily. An acrylic rod specified in ASTM E-2075 (17) can be used by mounting a transmitter at the designated SUT position (at one end of the rod) and machining a flat on the side of the rod for SUT installation.

11. Laser characterization of transmitting transducers should be repeated at a regular interval (of 1 to 3 years) for commercial usage. For our own transducers, the transmitting sensitivities appear to be stable over several years with intermittent use.

#### **4.2 SUT (receiver) and its characterization**

1. An SUT is to be acoustically coupled to a calibrated transmitter in a mechanically stable manner under adequate force of 10 to 50 N for the direct contact method (6,7). For the guided wave calibration, a similar coupling is done at the pre-selected position on a buffer medium (bar or plate). A suitable couplant must be applied to form a thin layer between the SUT and transmitter.

2. Machine oil and petroleum gel have given satisfactory performance, while silicone grease tends to be too viscous, making it difficult to achieve optimum coupling conditions. Even with petroleum gel like Vaseline requires 15 to 30 min to reach a stable condition at room temperature and receiver output continues to increase overnight. On the other hand, low viscosity couplant like motor oil can run out when uneven force is applied, leaving poor coupling conditions. Solid joint with a glue is stable, but couplant layer thickness is larger (18) and should be avoided >100 kHz.

3. After SUT-transmitter coupling is established, the transmitter is excited and SUT output is measured. Digitization parameters should be identical to those used for transmitter measurements to allow consistent spectrum operations of multiplication and division (or addition and subtraction in decibel scale). The length of recorded pulse signals needs to be selected according to the lowest frequency to be calibrated (16).

4. A suitable input impedance of digital oscilloscope must be chosen. For most applications, select the value corresponding to the input impedance of AE preamplifiers to be used. This is often 10 to 20 k-ohms. For low frequency AE sensors, such values result in severe sensitivity reduction. A long sensor cable also produces a similar effect. For these cases, it is recommended to use a short cable and high impedance input of 1 M-ohms as impedance and cable effects can be assessed separately (16).

5. When the frequency domain output is deduced from digitized receiver output, the receiver sensitivity can be obtained using the pulse transmitter input and transmitter sensitivity previously determined. In terms of decibel scale spectra, this operation is subtraction process. The output is in reference to 0 dB at 1 V/nm when the laser interferometer output gives displacement output in nm (6). Using a laser vibrometer that outputs in velocity or in m/s unit, one gets receiver sensitivity in reference to 1 V/m/s. Recent high-end laser vibrometers (e.g., Polytec PSV-400) also provide internally integrated displacement outputs. This part applies to both the direct contact and guided wave calibration methods.

6. Receiving displacement sensitivity obtained above can be converted to velocity or traditional pressure responses and vice versa (6).

7. When a buffer medium is desired in a modified direct contact method (e.g., for elevated temperature calibration), it is necessary to re-calibrate using a laser device or compensate for beam diffraction loss from the transmission sensitivity. Calculation for the diffraction loss is only available in closed form for identically sized transmitter and receiver, however (19). The buffer insertion should be avoided for low frequency sensors since the diffraction loss increases sharply at frequencies below 100 kHz.

8. A final note of caution is needed. The terms, "primary" and "absolute" calibration, have been used (2, 13). However, all the methods discussed here mount an SUT using a couplant and we have no means to characterize the couplant at present. It is also expected that the SUT mounting affects the vibration predicted theoretically or calibrated by a laser device, as noted in (2). Thus, it is perhaps more appropriate to use the term of sensitivity verification.

## 5. CONCLUDING REMARKS

This paper summarized information needed for standardization of AE sensor calibration using direct contact and guided wave methods. While some additional studies are required, these methods can verify the receiving sensitivity of AE sensors and are ready for standardization.

## REFERENCES

1. F.R. Breckenridge, C.E. Tschiegg, M. Greenspan, Acoustic emission: some applications of Lamb's problem, *J. Acoust. Soc. Am.*, 57, 626, 1975.
2. ASTM E1106-12 Standard test method for primary calibration of acoustic emission sensors, ASTM International, West Conshohocken, PA, USA, 2017, 12p.
3. ASTM E1781/E1781M-13 Standard practice for secondary calibration of acoustic emission sensors, ASTM International, West Conshohocken, PA, USA, 2013, 7p.
4. D. Eitzen and F.R. Breckenridge, NDT Handbook, vol. 6, Acoustic Emission Testing, ASNT, Columbus, OH, 2005, pp. 54-60.
5. H.L. Dunegan, Private communication, 2008.
6. K. Ono, Calibration methods of acoustic emission sensors. *Materials*, 9, 508, 2016.
7. Frequency Dependence of receiving sensitivity of ultrasonic transducers and acoustic emission sensors, *Sensors*, 18, 3861, 2018.
8. H. Vallen, Proposal for an absolute AE sensor calibration setup. Proc. World Conf. on Acoustic Emission, Xi'an, China, 11–13 October 2017.
9. H. Vallen, Obtaining AE sensor sensitivity curves verified by laser vibrometry, Proc. International Symp. on Acoustic Emission, XXIV, Sapporo, 5-9 Nov., Japanese Soc. for Non-Destructive Inspection: Tokyo, Japan, 2018, pp. 23-28.
10. K. Ono, T. Hayashi, H. Cho, Bar-wave calibration of acoustic emission sensors. *Appl. Sci.* 7, 964, 2017.
11. K. Ono, On the piezoelectric detection of guided ultrasonic waves. *Materials*, 10, 1325, 2017.
12. H. Hatano, T. Watanabe, Reciprocity calibration of acoustic emission transducers in Rayleigh-wave and longitudinal-wave sound fields. *J. Acoust. Soc. Am.*, 101, 1450–1455, 1997.
13. NDIS-2109-91, Method for absolute calibration of acoustic emission transducers by reciprocity techniques; Japanese Soc. for Non-Destructive Inspection: Tokyo, Japan, 1991; Revised 2004.
14. K. Ono, Critical examination of ultrasonic transducer characteristics and calibration methods. *Res. Nondestruct. Eval.* 28, 1–46, 2017.
15. R. Hill, N.L. Adams, Reinterpretation of the reciprocity theorem for the calibration of acoustic emission transducers operating on a solid. *Acustica*, 43, 305–312, 1979.
16. International Standard ISO 16063–11. Primary vibration calibrations by laser interferometry, International organization for standardization, Geneva, Switzerland, 1999.
17. ASTM E2075/E2075M-15 Standard practice for verifying the consistency of AE-sensor response using an acrylic rod, ASTM International, West Conshohocken, PA, USA, 2015, 5p,
18. K. Ono, Through-transmission characteristics of AE sensor couplants, *J. Acoust. Emiss.*, 34, 1-11, 2017.
19. P.H. Rogers, A.L. van Buren, An exact expression for the Lommel diffraction correction integral, *J. Acoust. Soc. Am.*, 55, 724, 1974.

# Transmitters for the face-to-face sensor sensitivity verification – is their scatter tolerable?

Hartmut Vallen  
Vallen Systeme GmbH, 82057 Icking, Germany, [www.vallen.de](http://www.vallen.de)

## ABSTRACT

In this work, “transmitter” (**TM**) means a device that converts a voltage to a particle motion. This work deals with differences of receiving sensitivity spectra (**Rv**) of an AE sensor under test (**SUT**), obtained by the face-to-face (**F2F**) method, when different TM units are used. It is an update of an earlier work in which a certain set-up of the F2F method was introduced. This work delivers a comparison of Rv spectra for three types of SUT, using alternatively three TM units of same type, and two FFT time windows of different length. Using the 50  $\mu$ s long window (W7) presents the resonances correctly in the Rv spectra, but the scatter of the Rv spectra (in terms of deviation from an average) is large. Using the 19  $\mu$ s long window (W1) presents resonance peaks 1-2 dB lower but the scatter is considerable lower. We would like to discuss the trade-off between the value of a lower scatter on cost of smoother resonance peaks in the Rv spectrum, and what level of scatter is considered tolerable.

**Keywords:** Acoustic emission sensor, sensor calibration, sensor sensitivity verification, scanning laser vibrometer.

## 1. INTRODUCTION

In an earlier work [1] we presented pairs of receiving sensitivity spectra of an AE sensor under test (**SUT**) using a pair of transmitters (either TMA or TMB, Olympus V104) in a face-to-face (**F2F**) setup. The principles and history of the F2F method is described in detail in Professor Ono’s systematic study of AE sensor calibration methods [2]. We reported deviations of up to 3,5 dB (peak-peak) in a pair of sensitivity spectra obtained for a wideband SUT (Olympus V103), and up to 7dB (peak-peak) for a 150 kHz resonant SUT (using FFT window W7). Several trials using different stimulations (sinewave, different pulse shapes) for compensating the deviations failed the objective. Meanwhile we received two more transmitter units (TMC, TMD) of same type. TMC fits best and was also used for this work. Since [1] reports in detail (downloadable) the used set-up, the following descriptions are reduced to the minimum needed for understanding the results, due to limited space.

## 2. MOTION MEASUREMENT BY USING A SCANNING LASER VIBROMETER

The output motion of each transmitter, stimulated by an electrical pulse, was measured by using a scanning laser vibrometer (**LVM**) at 161 positions at the transmitter face. The scanned positions were arranged in 10 rings of 16 positions per ring plus one in the center. One velocity signal versus time was obtained per circular area. Fig. 1 shows velocity signals of four circular areas stimulated by three transmitter (**TM**) units in one diagram per TM. Fig. 1 shows the main pulse at 10  $\mu$ s and a spike 8  $\mu$ s later, strongest in graph TMB-W6. This indicates a serious lack of uniformity of motion distribution at the face of TMB.

Velocity signal outputs from LVM and output signals of the SUT were subject to a window process with the purpose to exclude a part of the reverberation phase from the Fast Fourier Transform (**FFT**) process. In this work windows W6, W7 and later W1 are used. **W6** decays from 11  $\mu$ s to 16

$\mu\text{s}$  after pulse peak time, W7 from 50  $\mu\text{s}$  to 60  $\mu\text{s}$ , and W1 from 19  $\mu\text{s}$  to 21  $\mu\text{s}$ , smoothly, in the shape of half a cosine wave, from one to zero.

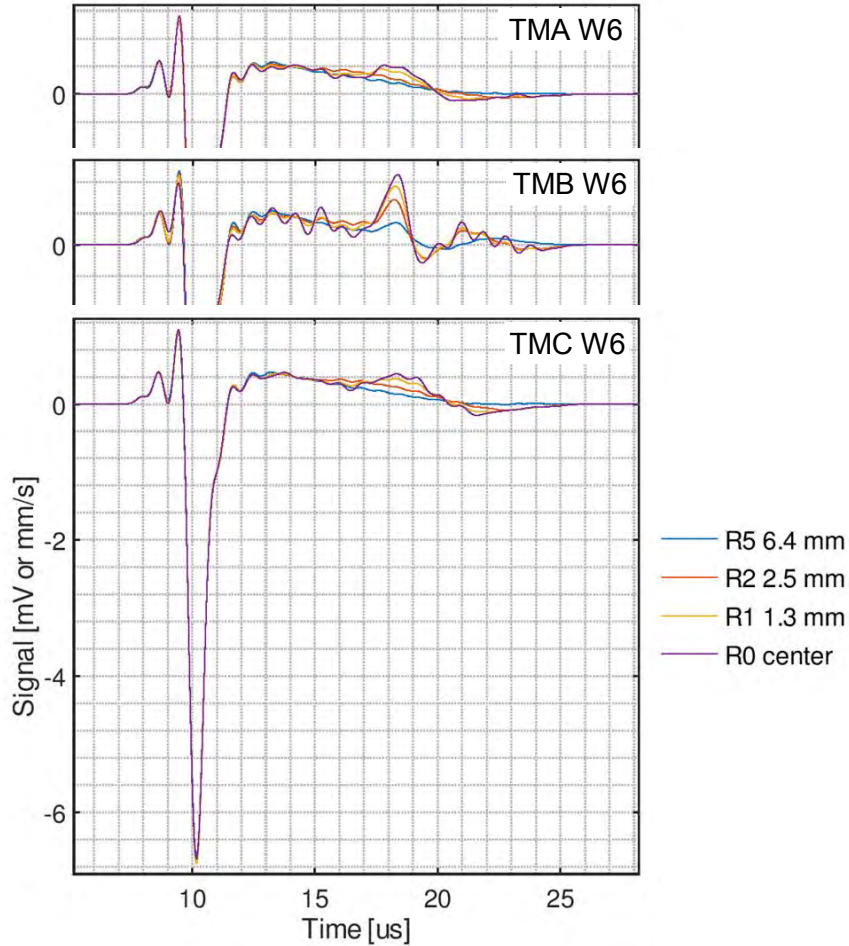


**Fig. 1** – Particle velocity diagrams for the circular areas defined by rings 5, 2, 1, 0 from transmitters TMA, TMB, TMC (top to down) using FFT window 6.

Windowing means multiplication of the signal to be processed by the window signal. The legend on the right of Fig. 1 shows the radii of the circle areas the velocity signals R0, R1, R2, R5 represent. The spike at 18  $\mu\text{s}$ , strongest with TMB, indicates some non-uniform motion distribution over the face of TMB.

### 3. FACE TO FACE SETUP

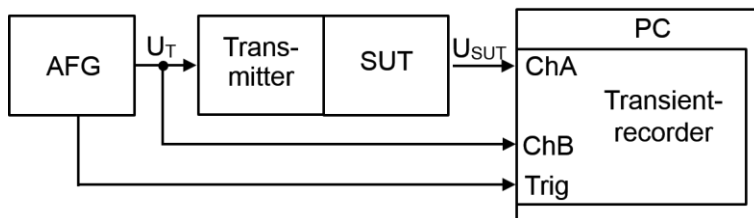


**Fig. 2** - Block diagram of face-to-face setup

Fig. 2 shows the block diagram of the face-to-face setup. The arbitrary function generator (AFG) delivers the voltage pulse  $U_T$  to the TM, causing a transient motion which is converted by the SUT

to the output voltage  $U_{SUT}$ . Both,  $U_{SUT}$  and  $U_T$ , are measured by a transient recorder. Equation (3) in [2] can be converted to:

$$U_{SUT} = U_T + Rv + Tv \quad (1)$$

$$Tv = V - U_{TL} \quad (2)$$

this leads to

$$Rv = (U_{SUT} - V) + (U_{TL} - U_T). \quad (3)$$

Each variable in equations (1) to (3) addresses a spectrum in dB where 0 dB refers to 1 [unit] given below:

$U_{SUT}, U_T$	SUT output voltage and TM input voltage in F2F setup in [V]
$Rv$	SUT's particle velocity receiving sensitivity in [V/(mm/s)],
$Tv$	TM's particle velocity transfer function in [(mm/s)/V]
$V$	particle velocity (measured by LVM) in [mm/s]
$U_{TL}$	Voltage spectrum at transmitter during velocity measurement in [V].

For more details see [1] and [2].

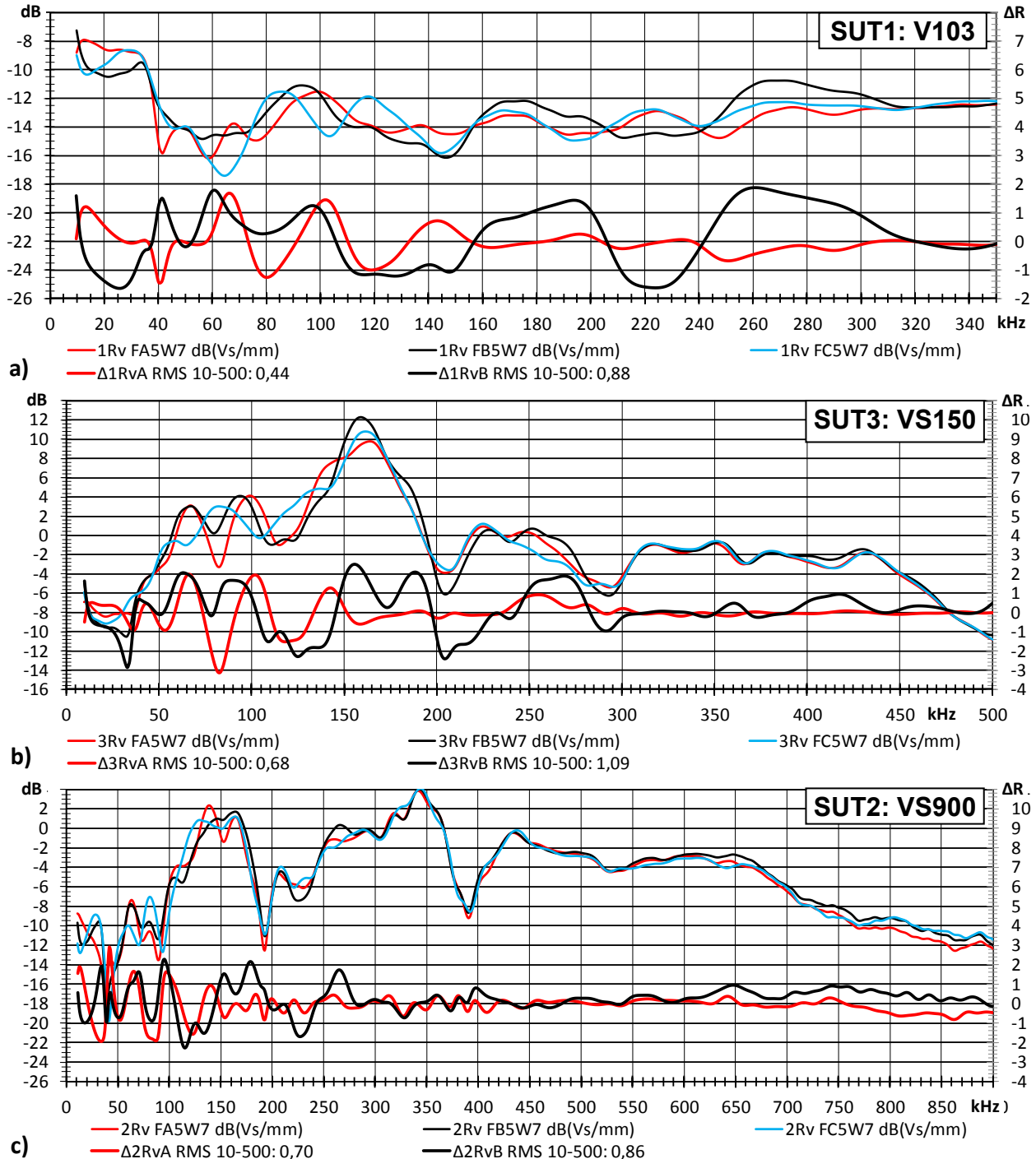
#### 4. RESULTS

The upper curve triplets in each diagram of Fig. 3 visualize for one SUT three receiving sensitivities  $RvA$ , (red, legend says 1Rv FA5W7),  $RvB$  (black), and  $RvC$  (blue), stimulated by three TM units A, B, C of same model (Olympus V104), scaled on the left axis. The right axis scale is for the lower pair of curves, identified by  $\Delta RvA$  (red) and  $\Delta RvB$  (black).  $\Delta RvA$  and  $\Delta RvB$  are deviations-from-average of  $RvA$  and  $RvC$ , in dB:  $\Delta RvA = RvA - (RvA + RvC)/2$  and  $\Delta RvB = RvB - (RvA + RvC)/2$ .  $RvB$  is excluded from the average because TMB causes too large deviations and is not qualified for this method. Since only  $RvA$  and  $RvC$  are averaged,  $\Delta RvC$  always equals minus  $\Delta RvA$  and is not shown. The legends of the  $\Delta Rv$  spectra indicate Root Mean Square (**RMS**) values of the  $\Delta RvA$  and  $\Delta RvB$  over the frequency range 10 kHz to 500 kHz. Table 1 summarizes the RMS and peak-peak values.

**Table 1** - Sensitivity deviations  $\Delta RvT$  of 3 SUT types stimulated by 3 TMs using 2 windows.

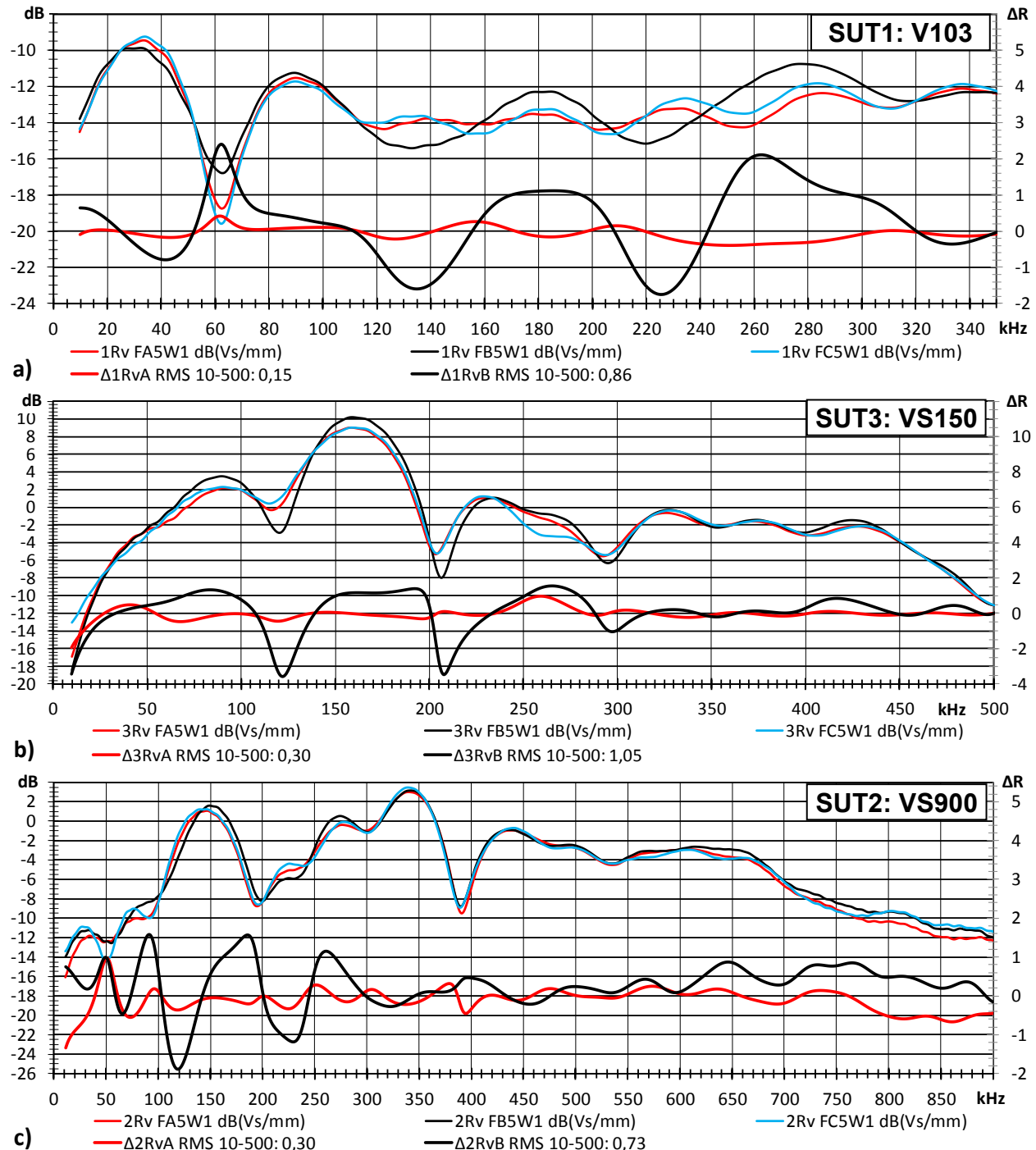
<b>SUT</b>		<b>RMS values</b>		<b>peak-peak values</b>	
<b>Fig.</b>	<b>Type</b>	<b><math>\Delta RvA</math></b>	<b><math>\Delta RvB</math></b>	<b><math>\Delta RvA</math></b>	<b><math>\Delta RvB</math></b>
3a)	V103	0,44	0,88	3,00	3,60
3b)	VS150	0,68	0,72	5,10	3,20
3c)	VS900	0,70	0,86	5,00	4,40
<b>ØW7</b>		<b>0,61</b>	<b>0,82</b>	<b>4,37</b>	<b>3,73</b>
4a)	V103	0,15	0,86	0,70	4,30
4b)	VS150	0,30	1,05	1,50	5,00
4c)	VS900	0,30	0,73	1,60	3,50
<b>ØW1</b>		<b>0,25</b>	<b>0,88</b>	<b>1,27</b>	<b>4,27</b>

Table 1 shows a substantial decrease of deviation in the sensitivity spectra when window W1 is used instead of window W7.



**Fig. 3 – RvT spectra (left scale) and  $\Delta$ RvT spectra (right scale) obtained from SUT a) V103-64, b) VS150M-6379, c) VS900M-4464 by using TMs A, B, C, and window W7 (50  $\mu$ s)**

Fig. 4 is similar to Fig. 3, but instead of window W7 (50  $\mu$ s), window W1 (19  $\mu$ s) was used. Since in both, Fig. 3a) and 4a), all  $\Delta$ Rv values above 320 kHz were low, the frequency range shown for the wideband sensor V103 was limited to the range 0 to 350 kHz for better low-end resolution. In Fig. 4 the red and blue curves are closer together and the RMS values in the legend of the red  $\Delta$ RvA are smaller than that of the black  $\Delta$ RvB.



**Fig. 4 – Rv spectra (left scale) and ΔRv deviation spectra (right scale) obtained from sensor  
a) V103-64, b) VS150M-6379, c) VS900M-4464 by using transmitters TMA, TMB, TMC.**

Fig. 5 shows per TM the ΔRvT spectra averaged over three SUTs, a) using W7 (50 µs, the data shown in Fig 3) and b) using W1 (19 µs, the data shown in Fig. 4).

In Fig. 5a) the deviation spectra in red and blue are as large as in black. Fig. 5b) shows small deviations in red ( $\Delta RvA$ ) and blue ( $\Delta RvC$ , equal to  $-\Delta RvA$ ) and larger deviations in black ( $\Delta RvB$ ). This tells two facts: 1) Transmitters exhibiting poor motion distribution, such as measured with

TMB (see Fig. 1), and 2) the length of the signal's reverberation phase processed by FFT must be limited to a point in time before the signals begin to separate.

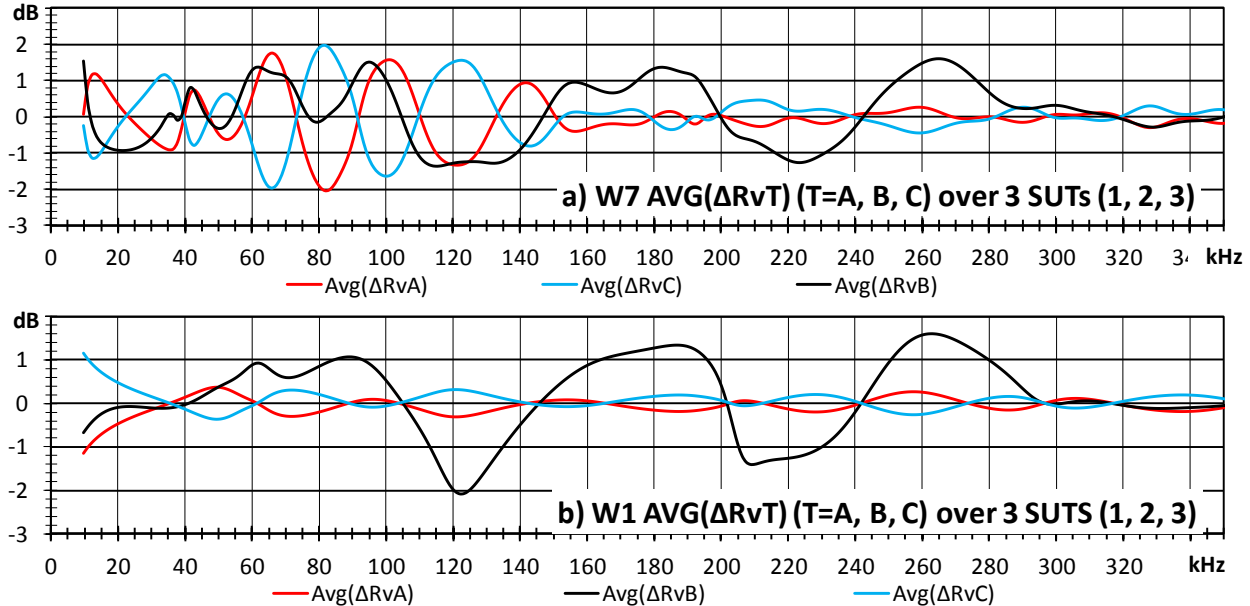


**Fig. 5** – The spectra shown are calculated by “ $Avg(\Delta RvT) = (\Delta 1RvT + \Delta 2RvT + \Delta 3RvT) / 3$ ”, with  $T=(A/B/C)$  and with “ $\Delta sRvT = sRvT - (sRvA + sRvC)/2$ ”, with  $s=(1/2/3)$  for the SUT.  
a) using window W7, b) W1.

Since amplitude and shape of the stimulation pulse was identical with each transmitter, the deviations in the sensitivity spectra must be caused by deviations of transmitter properties.

The following treats time domain signals of SUT1 (V103):

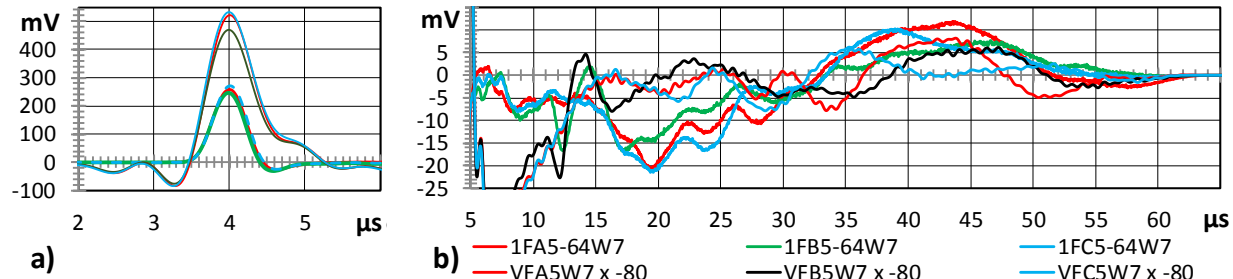


**Fig. 6** – SUT1 responses (thick), and velocity signals (thin) vs. time, from TMA (red), TMB (green), TMC (blue), a) main pulse at 4  $\mu s$ , b) zoomed reverberation phase.

Fig. 6a) shows the peak amplitudes at 4  $\mu s$ , about 260 mV of SUT output, 530 mV of velocity. Fig. 6b) shows the reverberation phase in a x16 amplitude zoom from 5 to 65  $\mu s$ .

The legends on the bottom of Fig. 6b) are common for both graphs. These legends begin with “1F” for SUT1 signals (V103), or “VF” for velocity signals (thinner curves, multiplied by 80, from LVM measurement). Third legend character (A/B/C for red/green/blue curve) identifies the used transmitter.

The velocity curves indicate the particle velocity in free air condition, the thicker curves the response of the SUT on the velocity input. The black (velocity) and green (SUT response) curves

of TMB show at 12  $\mu$ s a sharp rise, which obviously stems from the spike shown in Fig. 1, TMB-W6 at 18  $\mu$ s. This behavior disqualifies that TM exemplar.

From 5  $\mu$ s to 22  $\mu$ s the thicker red and blue curves (SUT responses) are close together. Then the curves develop differently. No relation between SUT response and velocity output of LVM can be seen. It seems, the SUT response is just reverberation of the main impulse.

In the F2F setup the tight acoustic coupling between SUT and transmitter combines the two piezo elements to one common element with specific resonance properties. These depend, amongst others, on the combined geometry. In addition to the mechanical load of the SUT on the TM the specific resonance properties may influence how the reverberation motion develops over time.

The following treats time and frequency domain signals of SUT3, a resonant 150 kHz sensor (VS150M-6379):

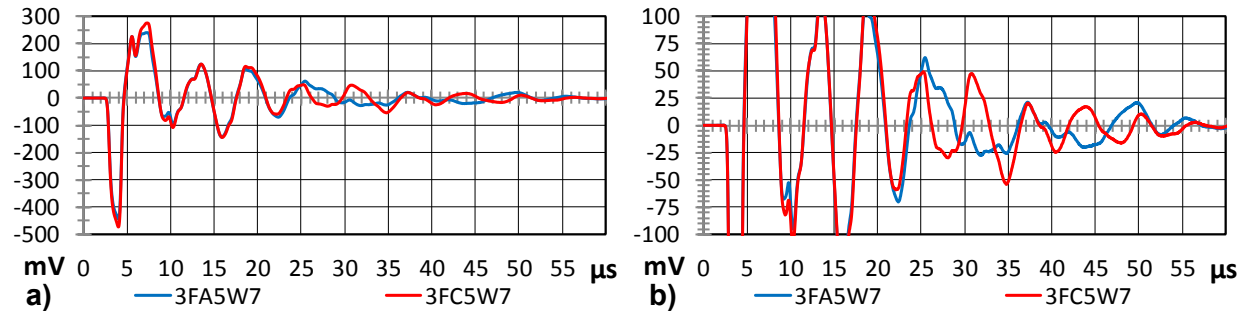


**Fig. 7 – Response of SUT3 on stimulation of TMA (blue) and TMC (red), a) normal scale, b) vertical zoom**

Fig 7 shows for SUT3 close curves up to 19  $\mu$ s after peak pulse time, as with SUT1 in Fig. 6, and then a different development of the response curves. This must be caused by a difference in properties of TMA and TMC. This fact caused that we introduced window W1 with 19  $\mu$ s length, while in [1] window W6 (11  $\mu$ s) was used.

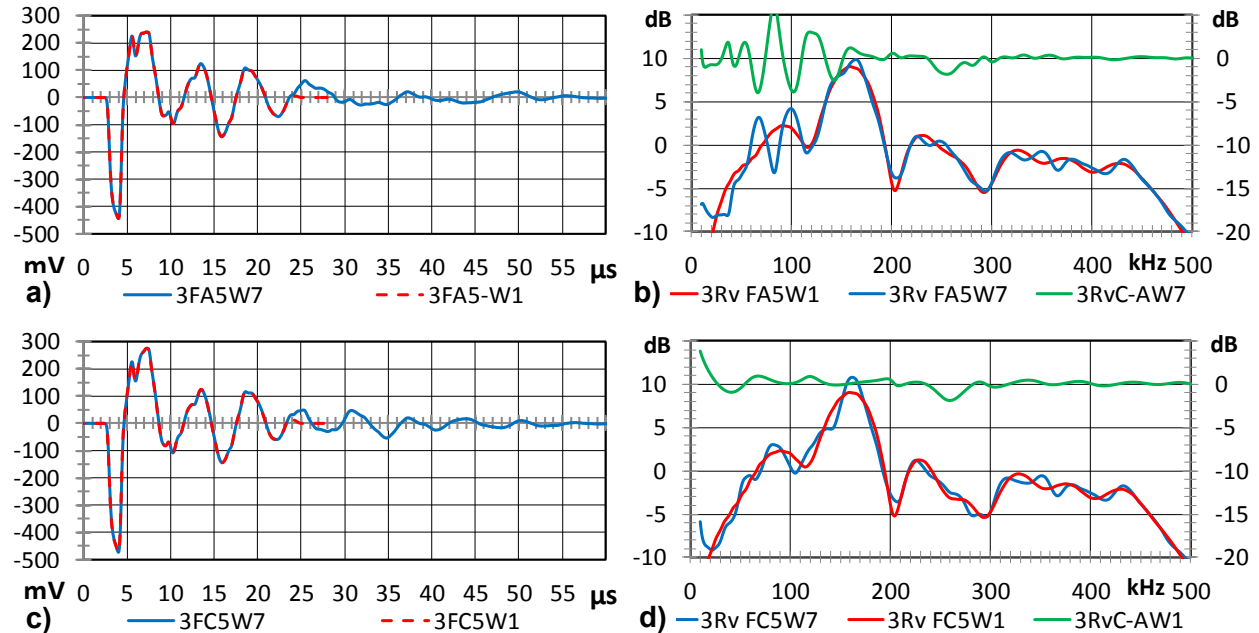


**Fig. 8 – W1 (red), W7 (blue); a, c) time domain; b, d) sensitivity in dB(Vs/m),  
Green curves: b) RvC - RvA using W7: large deviation; d) RvC - RvA using W1: small deviation.**

Fig. 8 d), green curve, proves that using window W1 and stimulation by TMA and TMC results in only small deviations. Blue and red curves prove that the reduction of peak sensitivity between use of W1 and W7 is small.

## 5. CONCLUSION

According to Table 1 the receiving sensitivity spectra, obtained by using two transmitter units (TMA and TMC), three SUT types, a 50  $\mu$ s long FFT window (W7), exhibit for the same SUT, deviation-from-average values ( $\Delta RvA$ ) up to 5 dB peak-peak, up to 0,9 dB RMS (root mean square, corresponds to standard deviation between Rv curves) and an average of 0,61 dB RMS.

By using a 19  $\mu$ s long window (W1), the deviation  $\Delta RvA$  is reduced from 0,61 dB to 0,25 dB RMS.

The use of window W1 smooths resonances to some extent. However, the peak maximum of the 150 kHz resonant sensor is only decreased by one to two dB between the use of W1 and W7.

The deviations  $\Delta RvB$  (when using a third transmitter TMB) are worse due to the TMB's disturbed motion distribution (Fig. 1, TMB W6).

We think the transmitter units must be selected for proper reproducibility of SUT stimulation. Only units with suitable uniformity of motion distribution should be used. A diagram like Fig. 7, showing a SUT1 response, would allow to discriminate best suited transmitters from others.

By LVM the free surface motion of the transmitter was measured. During stimulation the SUT is tightly coupled to the transmitter. It is obvious that the SUT coupling changes transmitter motion to some extent.

The F2F method stimulates uniform particle motion in normal direction. This corresponds to a longitudinal volume wave arriving at the volume's surface at the sensor position in normal direction.

If waves arrive at the sensor in other than the normal direction, or if Rayleigh or plate wave motions are passing by the sensor's sensitive area, the particle motion is not uniform and cancellation effects may happen in the sensor's piezo element and influence the apparent sensitivity spectrum of the sensor.

Even if reproducibility among TM units would be perfect the behavior of a SUT will change when it is moved from the F2F setup to a practical application, depending on the acoustic impedance of the material it is coupled to, but also on the geometry, the conditions of wave propagation and reflection.

The F2F method has potential to obtain a sensitivity spectrum under easy reproducible conditions, undisturbed by any mechanical interaction.

## 6. REFERENCES

- [1] Vallen, H. "AE sensor sensitivity verification using a stimulated motion, verified by laservibrometry", Proceedings of the EWGAE-33, Senlis, France, 12-14 September 2018, <https://www.ndt.net/article/ewgae2018/papers/21.pdf> (updated version)
- [2] K. Ono, "Calibration methods of acoustic emission sensors," Materials, 2016, 9, 508.